The SAMI Galaxy Survey: Environmental analysis of the orbital structures of passive galaxies

Giulia Santucci,[1,2,3]★ Sarah Brough,[1,3] Jesse van de Sande,[4,3] Richard McDermid, [5,3] Stefania Barsanti,[6,3] Joss Bland-Hawthorn,[4,3] Julia J. Bryant,[4,7,3] Scott M. Croom,[4,3] Claudia Lagos,[2,3] Jon S. Lawrence,[8] Matt S. Owers,[5,9,3] Glenn van de Ven, [10] Sam P. Vaughan,[4,11,3] Sukyoung K. Yi[12]

[1]*School of Physics, University of New South Wales, NSW 2052, Australia*
[2] *International Centre for Radio Astronomy Research (ICRAR), M468, University of Western Australia, 35 Stirling Hwy, Crawley, WA 6009, Australia*
[3]*ARC Centre of Excellence for All Sky Astrophysics in 3 Dimensions (ASTRO 3D), Australia*
[4]*Sydney Institute for Astronomy, School of Physics, University of Sydney, NSW 2006, Australia*
[5]*Department of Physics and Astronomy, Macquarie University, Sydney, NSW 2109, Australia*
[6]*Research School of Astronomy and Astrophysics, The Australian National University, Canberra, ACT 2611, Australia*
[7]*Australian Astronomical Optics, AAO-USydney, School of Physics, University of Sydney, NSW 2006, Australia*
[8]*Australian Astronomical Optics, Faculty of Science & Engineering, Macquarie University. 105 Delhi Rd, North Ryde, NSW 2113, Australia*
[9]*Astronomy, Astrophysics and Astrophotonics Research center, Macquarie University, Sydney, NSW 2109, Australia*
[10] *Department of Astrophysics, University of Vienna, Türkenschanzstrasse 17, 1180 Vienna, Austria*
[11]*Centre for Astrophysics and Supercomputing, School of Science, Swinburne University of Technology, Hawthorn, VIC 3122, Australia.*
[12]*Department of Astronomy and Yonsei University Observatory, Yonsei University, Seoul 03722, Republic of Korea*

Accepted XXX. Received YYY; in original form ZZZ

ABSTRACT
Most dynamical models of galaxies to date assume axisymmetry, which is not representative of a significant fraction of massive galaxies. We have built triaxial orbit-superposition Schwarzschild models of galaxies observed by the SAMI Galaxy Survey, in order to reconstruct their inner orbital structure and mass distribution. The sample consists of 153 passive galaxies with total stellar masses in the range $10^{9.5}$ to $10^{12} M_{\odot}$. We present an analysis of the internal structures and intrinsic properties of these galaxies as a function of their environment. We measure their environment using three proxies: central or satellite designation, halo mass and local 5^{th} nearest neighbour galaxy density. We find that although these intrinsic properties correlate most strongly with stellar mass, environment does play a secondary role: at fixed stellar mass, galaxies in the densest regions are more radially anisotropic. In addition, central galaxies, and galaxies in high local densities show lower values of edge-on spin parameter proxy $\lambda_{Re,EO}$. We also find suggestions of a possible trend of the fractions of orbits with environment for lower-mass galaxies (between $10^{9.5}$ and $10^{11} M_{\odot}$) such that, at fixed stellar mass, galaxies in higher local densities and halo mass have higher fractions of hot orbits and lower fractions of warm orbits. Our results demonstrate that after stellar mass, environment does play a role in shaping present-day passive galaxies.

Key words: galaxies: galaxy evolution - galaxies: kinematics and dynamics – galaxies: structure - galaxies: clusters: general - galaxies:group.

1 INTRODUCTION

Our current understanding of galaxy formation suggests that massive galaxies form in a two-phase process (e.g., Naab et al. 2009; Oser et al. 2010). During the first phase, at high redshift, they grow by a rapid episode of in-situ star formation, resulting in compact massive systems. After $z \approx 2$, these massive ($\log_{10}(M_*/M_{\odot}) > 10.5$) compact galaxies are predicted to be quiescent and grow mostly by accreting mass through galaxy mergers that add stars to their outskirts (e.g. Naab et al. 2009; Bezanson et al. 2009; Oser et al. 2010; van Dokkum et al. 2010; Wellons et al. 2016).

The ΛCDM model predicts a strong dependence of galaxy properties on their environment (e.g. Springel & Hernquist 2005), in particular because mergers are expected to play a vital role during the formation and/or evolution of almost every massive galaxy (e.g. White & Rees 1978). As interactions are more frequent for galaxies in groups compared to isolated galaxies, and since there are a number of physical mechanisms that may act in galaxy clusters to both trigger and truncate star formation in infalling galaxies (for example the interactions between the gas in the galaxy and the hot intracluster medium or the gravitational interactions between the galaxy and the cluster's gravitational potential - see Boselli & Gavazzi 2006; Cortese et al. 2021, for a review), a correlation between large-scale environment (groups and clusters, parametrised either as halo mass

---

★ E-mail: g.santucci@unsw.edu.au

or position within the halo) and galaxy properties is expected. In particular, central galaxies are expected to experience additional major mergers, due to their privileged position at the bottom of the potential well of groups (e.g. De Lucia & Blaizot 2007). Similarly, galaxies in dense environments, being exposed to more events that can affect their properties, are expected to show differences compared to galaxies of similar mass in low-density environments.

The merger history of a galaxy is thought to be one of the major factors that determines its internal kinematic structures (e.g., White 1979; Fall & Efstathiou 1980; Lagos et al. 2018b; Park et al. 2019; Lagos et al. 2022). Simulations of different combinations of minor and major mergers have been shown to lead to very different types of galaxies (e.g. Naab et al. 2014; Lagos et al. 2022). Therefore, we expect the internal orbital structures of central and satellite galaxies to show different characteristics if their merging histories are different. Simulations and observations to date have also shown that central galaxies tend to have more hot orbits and more prolate shapes (Tsatsi et al. 2017; Li et al. 2018) than satellite galaxies, consistent with this picture.

The advent of integral field spectroscopy (IFS) and large IFS surveys, such as ATLAS^{3D} (Cappellari et al. 2011a), the Sydney-AAO Multi-Object Integral-Field Spectrograph (SAMI) Galaxy Survey (Croom et al. 2012; Bryant et al. 2015), the Calar Alto Legacy Integral Field Area Survey (CALIFA; Sánchez et al. 2012), MASSIVE (Ma et al. 2014) and the Mapping Nearby Galaxies at Apache Point Observatory (MaNGA) survey (Bundy et al. 2015), have contributed to significantly expand our understanding of galaxy kinematics and their connection to intrinsic galaxy properties and their environment (e.g. Cappellari 2016).

IFS surveys have unveiled various correlations between the proxy for the spin parameter, $\lambda_{\rm Re}$, which provides a measurement of how rotationally supported a galaxy is, and galaxy properties for ETGs. For example, $\lambda_{\rm Re}$ is observed to be strongly correlated with stellar mass, so that the fraction of galaxies with low $\lambda_{\rm Re}$ (slow-rotating systems, i.e. galaxies whose kinematics are dominated by random motions) increases with increasing stellar mass (Emsellem et al. 2011; van de Sande et al. 2017b; Veale et al. 2017; Brough et al. 2017; Wang et al. 2020).

However, the results obtained from observations on the importance of the environment in shaping slow-rotating galaxies are contradictory. Central galaxies are generally found to be slow-rotating, with a spin parameter lower than that of other galaxies of the same stellar mass (Brough et al. 2011; Emsellem et al. 2011; Jimmy et al. 2013). D'Eugenio et al. (2013); Houghton et al. (2013); Scott et al. (2014); Fogarty et al. (2014); Cappellari (2016); Oliva-Altamirano et al. (2017); Brough et al. (2017); Rutherford et al. (2021) and van de Sande et al. (2021a) show that most slow-rotating galaxies live in high density environments, typical of massive groups or galaxy clusters. However, when galaxies were studied at fixed stellar mass, it was not clear whether this environmental trend held above the strong relationship with stellar mass (Veale et al. 2017; Brough et al. 2017; Greene et al. 2017; Wang et al. 2020). More recently, van de Sande et al. (2021a) found, using inclination-corrected λ_{Re} values for a large sample of galaxies with a range of morphologies, that among fast-rotating galaxies at fixed stellar mass, satellite galaxies have the lowest values of λ_{Re}, with isolated-central galaxies having the highest values and group/cluster centrals lying in-between. Similarly, galaxies in high-density environments have lower values of λ_{Re}, compared to those in low-density environments, at fixed stellar mass. This evidence points to stellar mass being the main driver of the evolution of the central regions of early-type galaxies from fast- to slow- rotating galaxies, with the environment playing a secondary role.

The observed λ_{Re} is directly calculated from observed kinematic maps and can only incorporate line-of-sight kinematics. Building triaxial orbit-superposition Schwarzschild models, we can separate dynamically-based derived properties of galaxies, such as intrinsic shape, orbital components, velocity anisotropy and inner mass distribution. These dynamical models can therefore provide more insight into the three-dimensional internal kinematic structures underlying the line-of-sight kinematics. Several different implementations of the Schwarzschild method, with varying degrees of symmetry, have been described (e.g. Cretton et al. 1999; Gebhardt et al. 2003; Valluri et al. 2004; van den Bosch et al. 2008a; Vasiliev & Athanassoula 2015; Vasiliev & Valluri 2020; Neureiter et al. 2021). The Schwarschild method has been used to study the internal stellar structure of gobular clusters (van de Ven et al. 2006; Feldmeier-Krause et al. 2017) and galaxies (e.g., Thomas et al. 2007; Cappellari et al. 2007; van de Ven et al. 2008; Feldmeier-Krause et al. 2017; Poci et al. 2019; Jin et al. 2020; Santucci et al. 2022; Pilawa et al. 2022), to model supermassive black holes (van der Marel et al. 1998; Verolme et al. 2002; Gebhardt et al. 2003; Valluri et al. 2004; Krajnović et al. 2009; Rusli et al. 2013; Seth et al. 2014; Thater et al. 2017, 2019; Liepold et al. 2020; Quenneville et al. 2021, 2022; Thater et al. 2022b), and has also been used to identify accreted galactic components (e.g., Zhu et al. 2020; Poci et al. 2021; Zhu et al. 2022). Zhu et al. (2018a) separated orbits into four different stellar components: a cold component with near circular orbits (with strong rotation), a hot component with near radial orbits (characterised by random motions), a warm component in-between (characterised by weak rotation) and a counter-rotating component (similar to the warm and cold components).

The number of studies focussed on the connection between the internal structure of galaxies and environment to date is very limited. Jin et al. (2020) analysed the intrinsic properties (orbital components, dark matter content and intrinsic shape) of 144 central and satellite early-type galaxies in the MaNGA survey, based on Schwarzschild models. They found no clear difference between the internal orbital structures of central and satellite galaxies. However, they found that, when considering the local density environments (indicated by neighbour counts), galaxies in denser regions tended to relatively have higher fractions of hot orbits.

In this paper we analyse triaxial dynamical model fits to SAMI Galaxy Survey data (Croom et al. 2012; Bryant et al. 2015; Owers et al. 2017; Croom et al. 2021) as a function of environment. We use properties derived from the Schwarzschild models in Santucci et al. (2022) to investigate the extent to which environmental processes affect internal galaxy structures and whether the evolutionary histories of central galaxies are different from those of satellite galaxies. SAMI Galaxy Survey data allow us to study the kinematic properties of a statistical sample of galaxies in a range of environments for the first time. The SAMI Galaxy Survey also allows us to better constrain the Schwarzschild models by providing information on the higher kinematic moments.

In Section 2 we describe the sample of galaxies and the data available for this analysis. Section 3 presents our results that are then discussed in Section 4. Our conclusions are given in Section 5. The SAMI Galaxy Survey adopts a ΛCDM cosmology with $\Omega_m = 0.3$, $\Omega_\Lambda = 0.7$, and $H_0 = 70$ km s^{-1} Mpc^{-1}.

2 DATA

2.1 SAMI

The Sydney-AAO Multi-object Integral field spectrograph (SAMI) Galaxy Survey is a large, optical Integral Field Spectroscopy (Croom et al. 2012; Bryant et al. 2015) survey of low-redshift ($0.04 < z < 0.095$) galaxies covering a broad range in stellar mass, $8 < \log_{10}(M_\star/M_\odot) < 12$, morphology and environment. The sample, with ≈ 3000 galaxies, is selected from the Galaxy and Mass Assembly Survey (GAMA survey; Driver et al. 2011) equatorial regions (group galaxies), as well as eight additional clusters to probe higher-density environments (Owers et al. 2017).

The SAMI instrument (Croom et al. 2012), on the 3.9m Anglo-Australian telescope, consists of 13 “hexabundles" (Bland-Hawthorn et al. 2011; Bryant et al. 2014), across a 1 degree field of view. Each hexabundle consists of 61 optical fibres that feed into the AAOmaga spectrograph (Sharp et al. 2006). In the typical configuration, 12 hexabundles are used to observe 12 science targets, with the 13th one allocated to a secondary standard star used for calibration. Moreover, SAMI also has 26 individual sky fibres, to enable accurate sky subtraction for all observations without the need to observe separate blank sky frames.

The raw telescope data is reduced into two cubes using the 2dfDR pipeline [1] together with a purposely written python pipeline for the later stages of reduction (Sharp et al. 2015).

SAMI data consist of 3D data cubes: two spatial dimensions and a third spectral dimension. The wavelength coverage is from 3750 to 5750 Å in the blue arm, and from 6300 to 7400 Å in the red arm, with a spectral resolution of R = 1812 (2.65 Å full-width half maximum; FWHM) and R = 4263 (1.61 Å FWHM), respectively (van de Sande et al. 2017b), so that two data cubes are produced for each galaxy target.

Each galaxy field was observed in a set of on average seven 30 minute exposures, that are aligned together by fitting the galaxy position within each hexabundle with a two-dimensional Gaussian and by fitting a simple empirical model describing the telescope offset and atmospheric refraction to the centroids. The exposures are then combined to produce a spectral cube with regular $0.5''$ spaxels, with a median seeing of $2.1''$. More details of the Data Release 3 reduction can be found in Croom et al. (2021)[2].

2.2 Schwarzschild models

In Santucci et al. (2022) we presented the orbit-superposition Schwarzschild model fits to a sample of 161 passive SAMI galaxies. Schwarzschild models allow us to model triaxial stellar systems in three steps: firstly we construct a model for the underlying gravitational potential of the galaxy; secondly we calculate a representative library of orbits in these gravitational potentials; and then we find a combination of orbits that can reproduce the observed kinematic maps and luminosity distribution. These steps are fully described in van den Bosch et al. (2008a) and Zhu et al. (2018b). We also corrected the orbital mirroring, as recommended by Quenneville et al. (2022), see also Thater et al. (2022a).

The underlying gravitational potential of the galaxy is constructed with a triaxial stellar component and a spherical dark matter halo. The triaxial stellar component mass is calculated from the best-fit two-dimensional Multi-Gaussian Expansion (MGE; Emsellem et al. 1994; Cappellari 2002) luminosity density (D’Eugenio et al. 2021). These MGE fits are calculated using $r-$band photometry from re-analysed Sloan Digital Sky Survey (SDSS; York et al. 2000) images for GAMA galaxies, reprocessed as described in Hill et al. (2011), as well as VST/ATLAS (VLT Survey Telescope - ATLAS; Shanks et al. 2015) and SDSS DR9 (Ahn et al. 2012) observations for cluster galaxies, with VST/ATLAS data reprocessed as described in Owers et al. (2017). Each best-fit two-dimensional MGE luminosity density is de-projected assuming the orientation in space of the galaxy, described by three viewing angles (θ, ϕ, ψ), to obtain a three-dimensional luminosity density. The space orientation (θ, ϕ, ψ) can be converted directly to the intrinsic shape, described by the parameters p, q, u. We leave p, q, u as free parameters to allow intrinsic triaxial shapes to be fitted. By multiplying a constant stellar mass-to-light ratio $M_\star/L$ (note that $M_\star/L$ is a free parameter in our modelling) by the 3D luminosity, we obtain the intrinsic mass density of stars.

A spherical Navarro-Frenk-White (NFW; Navarro et al. 1996) halo is adopted. The mass, M_{200} (mass enclosed within a radius, R_{200}, where the average density is 200 times the critical density), in a NFW dark matter halo is determined by two parameters, left free in our modelling. These are the concentration parameter, c, and the fraction of dark matter within R_{200}, $f = M_{200}/M_\star$ (where $M_\star$ is the total stellar mass). Our Schwarzschild implementation creates initial conditions for the orbits by sampling from the three integrals of motion (energy E, second integral I_2 and third integral I_3). Each set of orbits is sampled across the three integrals with the following number of points: $n_E \times n_{I_2} \times n_{I_3} = 21 \times 10 \times 7$. We tested increased sampling of the second integral I_2, for example increasing n_{I_2} from 10 to 18 and to 40, and re-fitting the models. The best-fit values retrieved by this test are consistent, within the 1σ confidence level, with the best-fit values retrieved by our regular runs. We therefore use three sets of $21 \times 10 \times 7$ orbits: a typical set of (E, I_2, I_3), a box orbits set (to compensate for the relatively low fraction of box orbits in the inner region present in the typical set) and a counter-rotating set of also (E, $-I_2$, I_3).

To test whether this number of orbits is enough to reproduce stable results, we select different sets of orbits, increasing n_E, n_{I_2} and n_{I_3}. We find that, although we see improvements, i.e. lower residuals in the surface brightness maps, when increasing the number of orbits from, for example $21 \times 10 \times 7$ to $31 \times 18 \times 9$, if we increase to $40 \times 18 \times 9$ there is an increase in the systematic residuals. We find that our derived results are stable if $n_E \times n_{I_2} \times n_{I_3}$ is set to $21 \times 10 \times 7$ or more. In addition, we test different orbital radial ranges for the sampling of the energy E and find that our fitted results are stable to the choice of radial range.

Once the orbit libraries are created, the orbit weights are determined by fitting the set of orbit-superposition models to the projected and de-projected luminosity density (from MGE fits) and the two-dimensional line-of-sight stellar kinematics (derived by van de Sande et al. 2017b,a). The model and the observed values are then divided by the observational error to undertake a χ^2 comparison. The weights are determined by the van den Bosch et al. (2008a) implementation, using the Lawson & Hanson (1974) non-negative least squares (NNLS) implementation. The best-fit model is defined as the model with minimum kinematic χ^2. In order to ensure that we get the best deprojection fit, we force the software to explore other regions of the parameter space (the parameter search easily gets stuck in local minima) by manually setting the parameters in areas that have yet to be explored. This way we are confident that we retrieve the values

---

[1] http://www.aao.gov.au/science/software/2dfdr; Croom et al. 2004; Sharp & Birchall 2010

[2] Reduced data-cubes and stellar kinematic data products for all galaxies are available on: https://datacentral.org.au.

for the global minimum. More details on the models set up for our sample can be found in Santucci et al. (2022).

2.2.1 Derived intrinsic properties

From these models we derived the internal orbital structure, inner mass distribution, intrinsic shape, velocity anisotropy and edge-on projected spin parameter $\lambda_{Re,EO}$ for each galaxy. In addition, following Zhu et al. (2018a), we separated orbits into four different components: a cold component with near circular orbits, a hot component with near radial orbits, a warm component in between and a counter-rotating component, according to their orbit circularity λ_z as following:

- cold orbits with $\lambda_z > 0.8$;
- warm orbits with $0.25 < \lambda_z < 0.8$;
- hot orbits with $-0.25 < \lambda_z < 0.25$;
- counter-rotating orbits with $\lambda_z < -0.25$

where $\lambda_z \equiv J_z/J_{max}(E)$ around the short z-axis, normalized by the maximum of a circular orbit with the same binding energy E. We calculated the fraction of orbits in each component within $1R_e$. We have derived dynamically-based intrinsic shapes using the triaxial parameter at $1R_\mathrm{e}$, $T_{Re} = (1-p_{Re}^2)/(1-q_{Re}^2)$, where p_{Re} and q_{Re} are the intermediate-to-long and short-to-long axis ratios. We separate galaxies into four groups according to this parameter: oblate ($T_{Re} \leq 0.1$), mildly triaxial ($0.1 < T_{Re} < 0.3$), triaxial ($0.3 \leq T_{Re} < 0.8$) and prolate ($T_{Re} \geq 0.8$). We have analysed the velocity anisotropy by defining the velocity anisotropy parameter in spherical coordinates, β_r, calculated within $1R_\mathrm{e}$, with $\beta_r > 0$ indicating radial anisotropy, $\beta_r < 0$ indicating tangential anisotropy and $\beta_r = 0$ indicating isotropy. Finally, we have reprojected the best-fit models to an edge-on view and measured, within $1R_\mathrm{e}$, the proxy for the spin parameter, $\lambda_{Re,EO}$. The measured $\lambda_{Re,EO}$ is consistent with the independently measured and inclination-corrected λ_{Re} measured directly from SAMI stellar kinematics by van de Sande et al. (2021a).

Uncertainties on the measured values are calculated using Monte Carlo realisations, combined with the 1σ confidence levels for the fluctuations from the best-fit model (as described in Santucci et al. 2022): we use the Monte Carlo realisation to investigate possible biases in this modelling as a result of using SAMI data, which generally has lower S/N and spatial resolution compared to the data used in previous analyses. We find typical uncertainties of ~10-15%.

We have explored how these parameters correlate with galaxy stellar mass in Santucci et al. (2022). In this paper we now analyse their connection to their environment, once the relationships with stellar mass are taken into account.

2.3 Stellar Mass

Stellar masses are estimated assuming a Chabrier (2003) initial mass function, from the $g-$ and the $i-$ magnitudes using an empirical proxy developed from GAMA photometry (Taylor et al. 2011; Bryant et al. 2015). For cluster galaxies, stellar masses are derived using the same approach (Owers et al. 2017). The $g-$ and $i-$ magnitudes are taken from SDSS images for GAMA galaxies and VST/ATLAS and SDSS DR9 observations for cluster galaxies.

2.4 Effective Radius

The effective radius, R_e, used here is that of the major axis in the r-band. The semi-major axis values were taken from MGE profile fits from the $r-$band photometry by D'Eugenio et al. (2021). The images used for the MGE fits are square cutouts with $400''$ side, centred on the centre of the galaxy, and the MGE fits are calculated using `MgeFit` (Cappellari 2002) and the regularisation feature described in Scott et al. (2009).

2.5 Environment measurements

In order to explore the role of the environment in shaping galaxy properties, we define three proxies for environment: halo mass, central/satellite/isolated and fifth nearest neighbour local environment density. Each of these are described below.

2.5.1 Halo mass

We use the GAMA Galaxy Group Catalogue (G^{3}C; Robotham et al. 2011) to define the galaxy groups in the GAMA (Driver et al. 2011) regions of the SAMI Galaxy Survey. In this catalogue, galaxies are grouped using an adaptive friends-of-friends (FoF) algorithm, taking advantage of the high spectroscopic completeness of the GAMA survey (~ 98.5%; Liske et al. 2015). For the GAMA groups we use the halo mass, M_{200}, the mass contained within R_{200} provided by GAMA. The halo mass was calculated from the group velocity dispersion, using:

$$\frac{M_{200}}{h^{-1}\,M_\odot} = \frac{A}{\frac{G}{M_\odot^{-1}\,\mathrm{km}^2\,\mathrm{s}^{-2}\,\mathrm{Mpc}}}\left(\frac{\sigma_\mathrm{FoF}}{\mathrm{km\ s}^{-1}}\right)^2 \frac{\mathrm{R}_\mathrm{FoF}}{h^{-1}\,\mathrm{Mpc}} \tag{1}$$

and then calibrated using a scaling factor, A, determined from comparison to haloes from simulated mock catalogues (see Robotham et al. 2011). G is the gravitational constant, $G = 4.301 \times 10^{-9}\ M_\odot^{-1}\ \mathrm{km}^2\ \mathrm{s}^{-2}$ Mpc, A is the scaling factor, σ_FoF is the velocity dispersion of the group and R_FoF is the projected radius of the group.

It is important to note that, following Owers et al. (2017), we apply a scaling factor of 1.25 to the cluster halo masses, due to calibration, to be consistent with the GAMA halo masses. We also scale the GAMA halo masses (defined using $H_0 = 100$ km s^{-1} Mpc^{-1}) to be consistent with the cosmology used here.

2.5.2 Central galaxies

We define the central galaxies as the most massive galaxy within $0.25\ R_{200}$ (e.g., Oliva-Altamirano et al. 2017; Santucci et al. 2020). To identify the central galaxies for the group sample, we check that the galaxy identified as the "iterative central" (Robotham et al. 2011) is also the most massive galaxy in the group. This is true for 66/67 groups in our sample. One group has a different galaxy selected as the iterative central and the most massive. For this group, we find that the most massive galaxy within a radius of $0.25\ R_{200}$ is the iterative central galaxy and we select it as the central galaxy.

A similar procedure is carried out to select the central galaxy in the clusters, in order to ensure consistency between the samples. We identify the galaxy that sits closest to the centre of the cluster (cluster centroids are taken from Owers et al. 2017) as well as the most massive galaxy in the cluster. For 3 out of 8 clusters, these galaxies are the same. For the other 5 clusters, we find the most massive galaxy within a radius of $0.25\ R_{200}$. For 2 clusters this galaxy is also the central one, whereas for 3 out of 5 clusters (Abell 168, Abell 2399 and Abell 4038) the most massive galaxy within $0.25\ R_{200}$ is not the galaxy closest to the centre. This is consistent with the dynamical state of these clusters as discussed in Owers et al. (2017) and Brough et al. (2017). We therefore select the most massive galaxy within 0.25 R_{200} as the central galaxy for these clusters.

All other galaxies in each halo are classified as satellite galaxies. Galaxies which do not belong to any halo, or which belong to haloes with only two members, are classified as isolated galaxies.

2.5.3 *Local galaxy density*

We determine the local environment of galaxies using a nearest-neighbour density estimate to probe the underlying density field, with the assumption that galaxies with closer neighbours are also in denser environments (e.g. Muldrew et al. 2012).

We use the fifth nearest-neighbour local surface density measurement, Σ_5, to quantify the local environment around SAMI galaxies (Brough et al. 2013, 2017; Croom et al. 2021). Σ_5 measurements for both GAMA and cluster galaxies are derived using the projected comoving distance to the 5th nearest neighbour (d_5^2) with a velocity limit $V_{\rm lim}$ = 1000 km s^{-1}, and $M_{\rm lim} = -18.5$ mag, so that all neighbors are within a volume-limited density-defining population that has absolute magnitudes $M_{\rm r} < M_{\rm lim} - Q_{\rm z}$ (we assume $Q_{\rm z} = 1.03$, which is defined as the expected evolution of $M_{\rm r}$ as a function of redshift; Loveday et al. 2015):

$$\Sigma_5 = \frac{5}{\pi d_5^2} \tag{2}$$

In GAMA, galaxies for which the fifth nearest neighbour is more distant than the nearest survey boundary may have erroneous environment density measurements. None of the galaxies in our sample have measurements of Σ_5 affected by this problem.

2.6 Sample Selection

For this analysis we are particularly interested in whether there is an environmental dependence to the evolution of passive galaxies. We focus on the passive galaxies to determine how their environment affects their internal orbital structures. For this reason, we select the 161 SAMI passive galaxies (selected using the SAMI spectroscopic classification presented in Owers et al. 2019) used in the analysis presented in Santucci et al. (2022). Galaxies with stellar masses below $\log_{10}(M_\star/M_\odot) = 9.5$ were excluded, because the incompleteness of the stellar kinematic sample is larger than 50% of the SAMI galaxy survey sample observed in this mass range, as well as galaxies where $R_{\rm e} < 2''$ (due to their spatial size being smaller than the instrumental spatial resolution). The galaxies in the final sample were selected as the optimal compromise between best quality data and reasonable sample size and correspond to galaxies with 85 Voronoi bins within $1R_{\rm e}$ and $R_{\rm max} > R_{\rm e}$.

Since the GAMA group sample includes all galaxy associations with two or more members, to ensure the robustness of our group sample we first select all the SAMI observed galaxies that belong to GAMA haloes with a robustly estimated velocity dispersion and therefore halo mass (i.e. $\sigma > \sigma_{err}$; Robotham et al. 2011). These cuts leave a sample of 146 galaxies. Of these, 37 are central and 90 are satellite galaxies and 19 are isolated galaxies (i.e. not assigned to any group).

In order to further probe the cluster environment, we select an additional 7 central cluster galaxies, whose kinematic measurements did not reach 1 $R_{\rm e}$. Since the measurements for these galaxies did not meet our radial coverage criterion (outlined in van de Sande et al. 2017b; Santucci et al. 2022), larger uncertainties have been applied to their derived intrinsic properties from the Schwarzschild modelling (see Appendix A in Santucci et al. 2022).

This inclusion gives us a final sample of 153 SAMI galaxies, including 44 central galaxies, 90 satellite galaxies and 19 isolated galaxies. These are shown in Fig. 1 and used hereafter in this analysis.

3 INTRINSIC PROPERTIES OF GALAXIES AS FUNCTION OF ENVIRONMENT

To explore the role of environment in shaping the intrinsic properties of galaxies, we first divide the sample as follows: central (44 galaxies), satellite (90 galaxies) and isolated (19 galaxies). Each of these have been divided into four mass bins, with an equal number of galaxies in each (11 for centrals, 22 for satellites and 5 for isolated galaxies) In Sec. 3.1 we show how intrinsic properties such as edge-on projected $\lambda_{Re,EO}$, triaxiality, velocity anisotropy and fraction of orbits change with galaxy designation. We then explore how these properties and the fractions of orbits are distributed in the halo mass-stellar mass and local density-stellar mass planes in Sec. 3.2. We show the distribution of the galaxies in our sample with halo mass (panel a) and local density (panel b) in Fig. 2.

3.1 Intrinsic properties of central, satellite and isolated galaxies

We present the spin parameter measured from the reprojected edge-on maps $\lambda_{Re,EO}$ as a function of stellar mass in Fig. 3, panel a. Dividing the galaxies into central, satellite and isolated galaxies, we find suggestions that at fixed stellar mass (for galaxies with $\log M_\star/M_\odot \geq 11$), central galaxies have consistently lower mean values of $\lambda_{Re,EO}$ than satellite galaxies, which do not show any trend of $\lambda_{Re,EO}$ with stellar mass. We note, however, that the mass range where these satellite and central galaxies overlap is small. Isolated and central galaxies are more slowly rotating with increasing stellar mass.

We then explore galaxy triaxiality as a function of stellar mass for central, satellite and isolated galaxies in Fig. 3, panel b. Central galaxies are more likely to be triaxial (14% ± 5% of the central galaxies have $T_{Re} > 0.3$), compared to satellite and isolated galaxies (7% ± 3% and 5% ± 4%, respectively). However, this increase in the fractions of triaxial shapes for central galaxies is likely driven by the stellar mass as more massive galaxies have higher mean triaxiality (as also seen in Jin et al. 2020, Fig. 11, and Santucci et al. 2022, Fig. 8). We also note that the three most prolate-like galaxies in our sample are satellite galaxies.

In Fig. 3, panel c, we show the velocity anisotropy parameter in spherical coordinates, β_r, calculated within $1R_e$ as described in Santucci et al. (2022), as a function of stellar mass for central/satellite/isolated galaxies. $\beta_r > 0$ indicates that the galaxy is dominated by radial anisotropy, $\beta_r < 0$ indicates tangential anisotropy and $\beta_r = 0$ indicates isotropy. We find that, at fixed stellar mass, central galaxies are generally more radially anisotropic than satellite galaxies and that isolated galaxies show lower values of β_r (more tangentially anisotropic) than satellite galaxies, but no difference is found at stellar masses greater than $\log\ M_\star/M_\odot \sim 10.75$.

In Santucci et al. (2022), we divided each galaxy into four orbital components, according to their orbit circularity distribution (cold, warm, hot and counter-rotating components), calculating the fraction of each component within $1R_e$. We show the four orbital fractions as a function of stellar mass divided into central, satellite and isolated galaxies in Fig. 4. Central galaxies have the lowest fractions of warm orbits and the largest fractions of hot orbits at all masses. At fixed

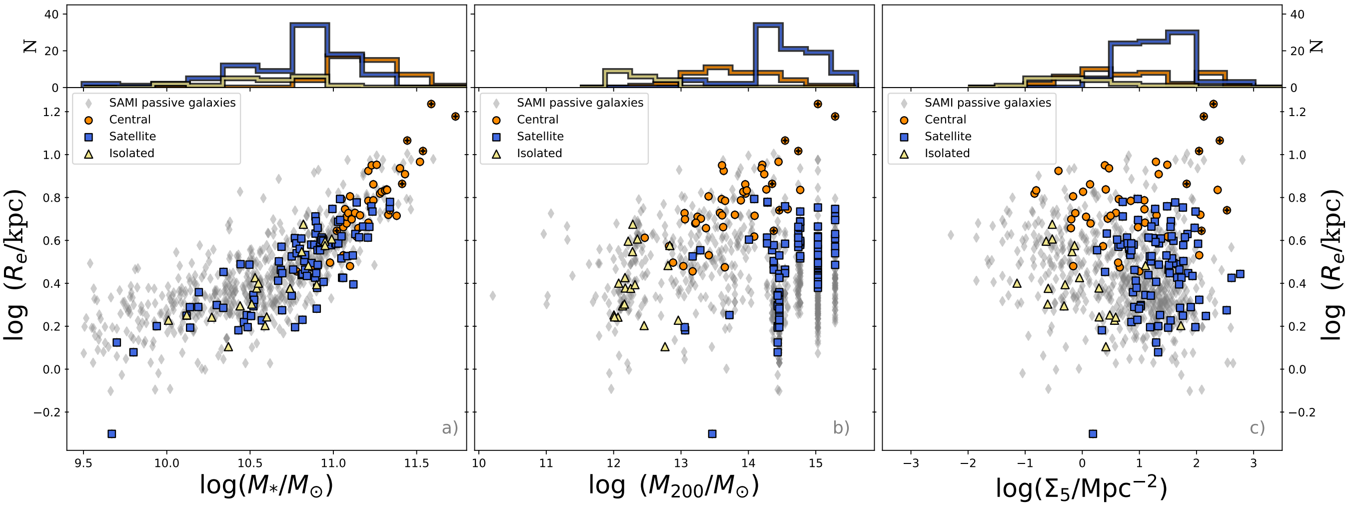

Figure 1. Effective radius, R_e, versus stellar mass (panel a), halo mass (panel b) and local density (panel c). Grey diamonds are the passive galaxies in the SAMI sample with $\log_{10}(M_\star/M_\odot) > 9.5$ and $R_e > 2''$ (738), orange circles are central galaxies (44), blue squares are satellite galaxies (90) and yellow triangles are isolated galaxies (19) in our SAMI sample. The additional 7 central cluster galaxies, whose kinematic measurements did not meet our radial coverage criterion, are highlighted with black crosses. Top panels show the distribution of central/satellite/isolated galaxies in stellar mass, halo mass and local density.

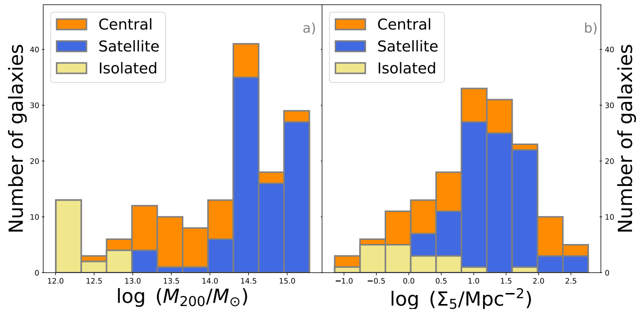

Figure 2. Distribution of halo mass (log $M_{200}/M_\odot$, panel a) and local density (log Σ_5, panel b) for the galaxies in our sample. The cumulative histograms are colour-coded by galaxy designation (central, satellite or isolated).

stellar mass, central galaxies have slightly lower mean fractions of warm orbits, compared to satellite and isolated galaxies of similar mass. No other significant difference is found between the orbital fractions of central, satellite and isolated galaxies.

3.2 Environment-stellar mass plane

To better visualise the potential trends with environment, we now explore the distribution of the edge-on projected $\lambda_{Re,EO}$, triaxiality, velocity anisotropy and orbital fractions in the halo mass-stellar mass and local density-stellar mass planes, in order to constrain the role of the environment once the relationship between these parameters and stellar mass is taken into account.

3.2.1 Spin parameter

We explore the environmental dependence of the spin parameter measured from the reprojected edge-on maps $\lambda_{Re,EO}$ as a function of stellar mass and environment in Fig. 5, colour-coding the galaxies by their edge-on spin parameter $\lambda_{Re,EO}$. We apply a locally weighted regression algorithm (LOESS - Cappellari et al. 2013) to the data to recover any mean underlying trend. Native figures are presented in Appendix A, for completeness. In order to quantify the trends with environment, we calculate the Spearman's semi-partial correlation coefficient, ρ, using the Python package *pinguoin.partial_corr* (Vallat 2018). This allows us to calculate the strength of a correlation of our parameters ($\lambda_{Re,EO}$, in this case) with the environment, taking into account the contribution from stellar mass, and to determine how likely it is that any observed correlation is due to chance. A ρ value close to 1 indicates a strong correlation, while a value close to -1 indicates a strong anti-correlation [3]. At fixed stellar mass, for masses above $\log M_\star/M_\odot \sim 11$, there is a suggestion of a relationship between $\lambda_{Re,EO}$ and halo mass so that galaxies in lower-mass haloes are less rotationally supported (Spearman's semi-partial correlation coefficient ρ = - 0.22, significant at the 1σ level, with a p-value of 0.084). This region of the stellar mass - halo mass plane is dominated by central galaxies, which are, at fixed stellar mass, less rotationally supported (as seen in Fig. 3), suggesting that this trend is likely be driven by the central/satellite/isolated designation. For galaxies with stellar masses below $\log M_\star/M_\odot \sim 11$ we do not find any significant correlation with halo mass. When looking at the trends with local density we find that, at stellar mass $\log M_\star/M_\odot < 11$, $\lambda_{Re,EO}$ decreases with increasing local density (ρ = -0.27, significant at the 1σ level, with a p-value of 0.097), so that we see suggestions that galaxies in higher local densities are less rotationally supported than galaxies in less dense regions.

3.2.2 Intrinsic shape

We show the distribution of galaxy triaxiality in the halo mass-stellar mass and local density-stellar mass plane in Appendix B, Fig. B1. In both cases, we do not find any significant correlation between triaxiality and environment.

---

[3] We present all relationships with probabilities 1-σ or greater, as these analyses are among the firsts of their kind, although the sample is small for bimodal statistics. We note that even though the relationships do not show strong correlations, they are important to guide future analyses.

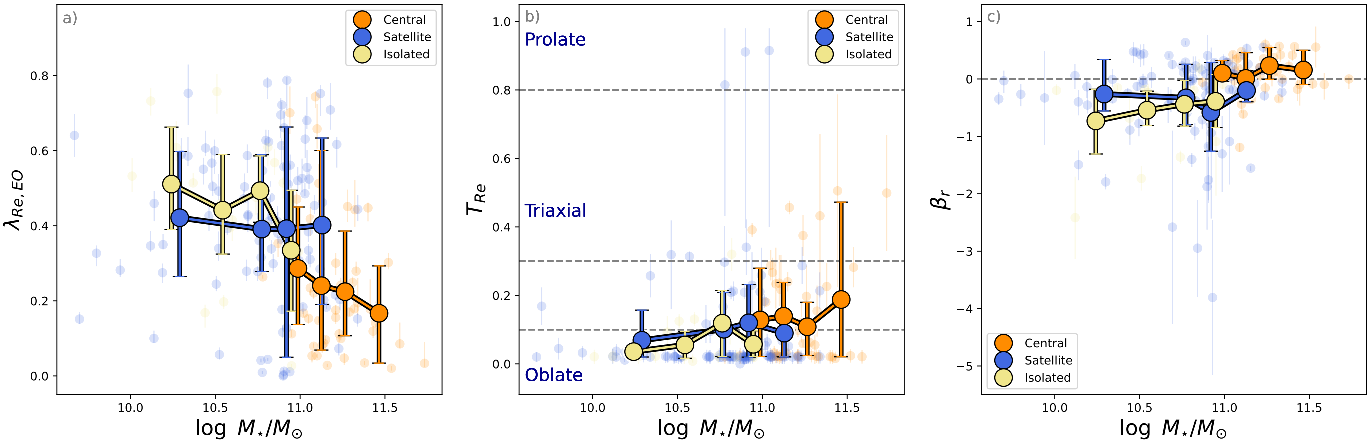

Figure 3. Spin parameter $\lambda_{Re,EO}$ (panel a), , triaxiality T_{Re} (panel b) and velocity anisotropy β_r (panel c) as a function of stellar mass. The mean values of $\lambda_{Re,EO}$, T_{Re} and β_r for 4 mass bins are shown as large circles, colour-coded by central/satellite/isolated designation. Bold error bars represent the 1σ scatter around the mean value of each mass bin. At fixed stellar mass, central galaxies have consistently lower mean values of $\lambda_{Re,EO}$ than satellite galaxies, and show a strong trend with stellar mass. Central galaxies are more likely to be triaxial than satellite and isolated galaxies and they are dominated by radial anisotropy. Satellite galaxies do not show any trend of $\lambda_{Re,EO}$, or T_{Re}, with mass. Satellite and isolated galaxies are dominated by tangential anisotropy.

3.2.3 *Velocity anisotropy*

We explore the distribution of our galaxies in halo mass in Fig. 6 (panel a) and local density (panel b) as a function of stellar mass, colour-coding the galaxies by their velocity anisotropy and LOESS smoothed to recover any mean underlying trend.

At fixed environmental proxy, β_r increases with increasing stellar mass. We find some hints that the most radially anisotropic galaxies are in mid-mass haloes. This could be a selection effect, since the most radially anisotropic galaxies are central galaxies and we only have 8 central galaxies in clusters (out of 44 central galaxies in the sample, e.g. Fig. 3, panel c). For galaxies with stellar masses below $\log\ M_\star/M_\odot \sim 11$, we find a value of $\rho = 0.19$ for a correlation between β_r and halo mass taking stellar mass into account. This is significant at the 1-σ level (with a p-value of 0.767). For local density (panel b), we find evidence of a correlation of β_r with environment so that at fixed stellar mass galaxies in higher local densities have greater values of β_r, particularly visible for galaxies with stellar masses $\log\ M_\star/M_\odot < 11$. We find $\rho = 0.33$ for a correlation between β_r and local density - significant at the 2-σ level (with a p-value o 0.035). This suggests the possibility of a weak positive correlation between velocity anisotropy and halo mass and local density such that velocity dispersion anisotropy increases with increasing environmental density.

3.2.4 *Orbital components*

We now explore the distribution of the fraction of orbits in the halo mass-stellar mass and local density-stellar mass planes. We show halo mass (panel a) and local density (panel b) as a function of stellar mass, colour-coded by the fraction of warm orbits in Fig. 7 and hot orbits in Fig. 8.

We find suggestions of a possible relationship between the fraction of warm orbits and environment (Fig. 7), so that, at fixed stellar mass, the fraction of warm orbits for galaxies with stellar mass below $\log M_\star/M_\odot \sim 11$ decreases with increasing halo mass and increasing local density. The Spearman's semi-partial correlation coefficient gives a suggestion of a trend ($\rho = -0.19$ at the 1-σ level, with a p-value of 0.077) for the fraction of warm orbits with local density.

For stellar masses below $\log M_{star}/M_\odot \sim 11$, galaxies show evidence of a possible additional relationship between the fraction of hot orbits and environment so that galaxies in higher-mass haloes and denser local environments are more likely to have higher fractions of hot orbits (Fig. 8). Testing the correlation of the fractions of hot orbits for galaxies with stellar mass below $\log M_{star}/M_\odot \sim 11$ we find a Spearman's semi-partial correlation coefficient $\rho = 0.22$ at the 1-σ level, with a p-value of 0.18 with halo mass, and $\rho = 0.18$ at the 1-σ level, with a p-value of 0.089, when considering the local density.

We do not find any additional correlation between the fraction of cold/counter-rotating orbits and halo mass or between the fraction of cold/counter-rotating orbits and local density. We show the distributions of the fraction of cold orbits in Fig. C1 and of the fraction of counter-rotating orbits in Fig. C2, in Appendix C for completeness.

4 DISCUSSION

We have explored the connection between environment and galaxy dynamically-derived properties such as intrinsic shape, velocity anisotropy and orbital components using three proxies for environment: central/satellite/isolated, halo mass and fifth nearest neighbour local environment density. We analysed a sample of 153 passive galaxies from the SAMI Galaxy Survey, which allows us to study dynamically-derived galaxy properties for a significant number of galaxies in a range of environments for the first time. Here we discuss how our results compare to the literature and possible evolution scenarios for passive galaxies..

4.1 Spin Parameter

Exploring the connection between the intrinsic edge-on λ_{Re} and the environment we found that galaxies in high local densities showed lower values of λ_{Re}, at fixed stellar mass, for galaxies with $\log M_\star/M_\odot < 11$ (Fig. 5). Moreover, central galaxies (with stellar

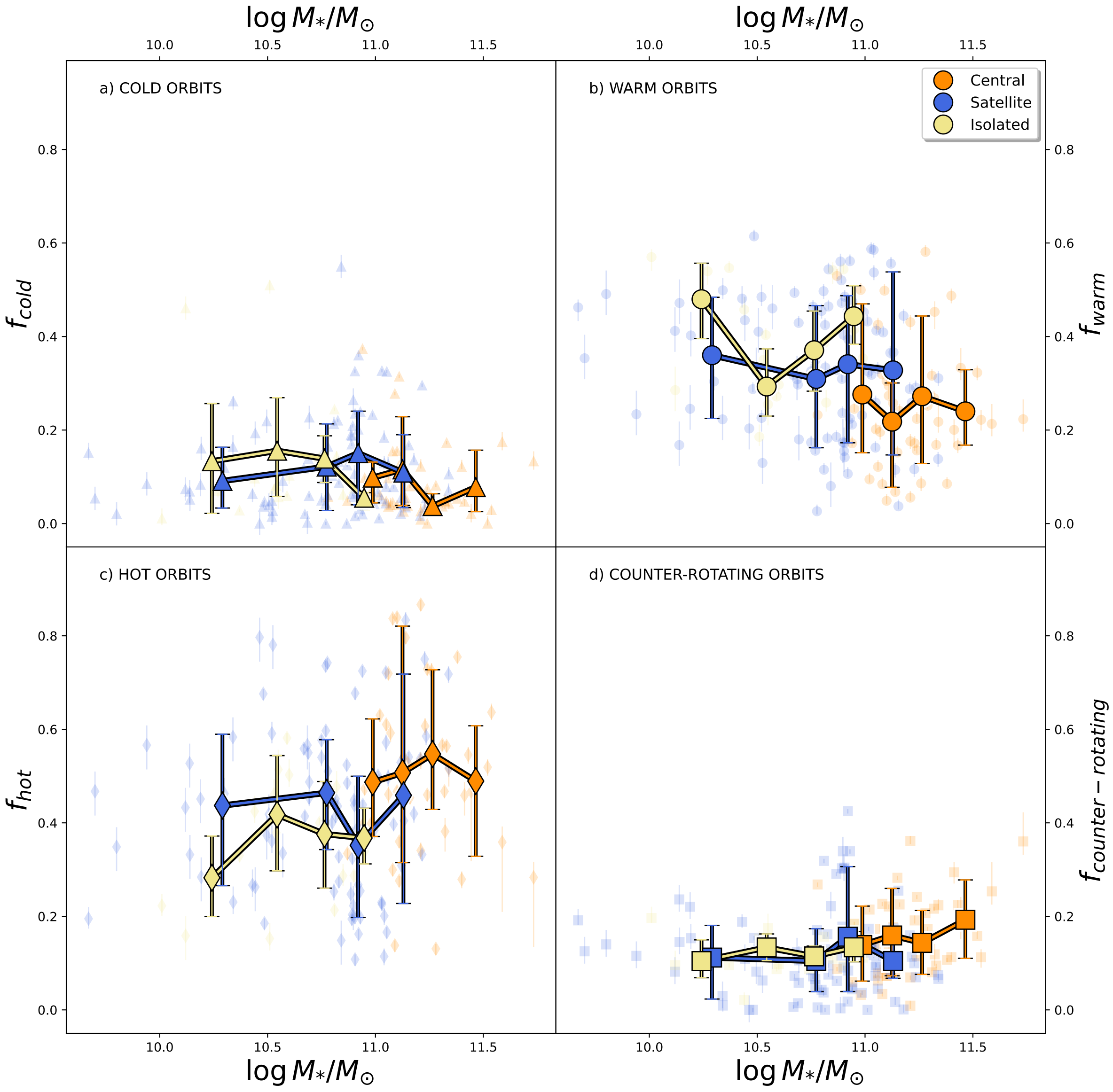

Figure 4. Fractions of: a) cold orbits, b) warm orbits, c) hot orbits and d) counter-rotating orbits as a function of stellar mass. Galaxies are classified into central (orange), satellite (blue) and isolated (yellow) galaxies. Each class is divided into 4 mass bins, with the bold points representing the mean values for each mass bin and the error bars indicate the 1σ scatter around the mean value. In general, central, satellite and isolated galaxies show similar trends for the fraction of orbits, with no significant difference, although at fixed stellar mass, central galaxies have the lowest fractions of warm orbits and the highest fractions of hot orbits.

mass $\log M_\star/M_\odot > 11$) have lower values of λ_{Re} than satellite galaxies of similar stellar mass (Fig. 3).

Previous results in the literature have found a strong dependence of λ_{Re} with stellar mass. However, there are contradictory results for whether the environment plays a role in shaping galaxies, in particular slow-rotating ones. Several studies found a higher fraction of slow-rotating galaxies in the densest environments (e.g Cappellari et al. 2011b; D'Eugenio et al. 2013; Scott et al. 2014; Fogarty et al. 2014). However, later studies controlled for stellar mass and found that the environment has no significant correlation with the fraction of slow-rotating galaxies (Brough et al. 2017; Veale et al. 2017; Green et al. 2018). These differences were resolved in van de Sande et al. (2021a) and explained by sample sizes and differences in selection and range in environment studied.

Our results are in agreement with van de Sande et al. (2021a), who derived the intrinsic values of λ_{Re} by applying corrections for seeing, aperture effects and inclination for ~ 1800 SAMI galaxies, including ETGs and LTGs, following Harborne et al. (2020). They found that central galaxies at stellar masses greater than $\log M_\star/M_\odot \sim 11$ are more likely to be slow-rotators than satellite galaxies in the same mass bin. Moreover, they also find a similar trend of λ_{Re} with local density as we observe here.

There is also evidence from simulations that points towards environmental dependence as a weaker secondary effect on λ_{Re}. For example, Lagos et al. (2018b), using IFS-like "observations" of syn-

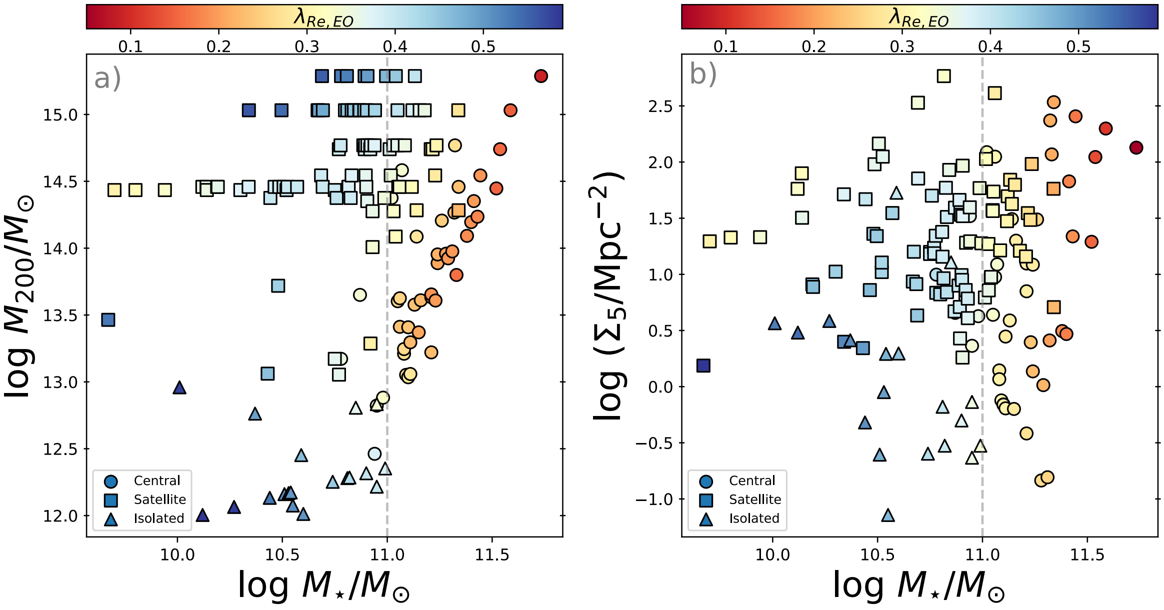

Figure 5. Halo mass log M_{200} and local density $\log(\Sigma_5/\mathrm{Mpc}^{-2})$ as a function of stellar mass, colour-coded by the intrinsic spin parameter $\lambda_{Re,EO}$, LOESS smoothed. We find that at fixed environment, $\lambda_{Re,EO}$ decreases with increasing stellar mass. At fixed stellar mass, for masses above $\log M_{\star}/M_{\odot} \sim 11$, there is weak evidence of a relationship between $\lambda_{Re,EO}$ and halo mass. $\lambda_{Re,EO}$ also decreases with increasing local density.

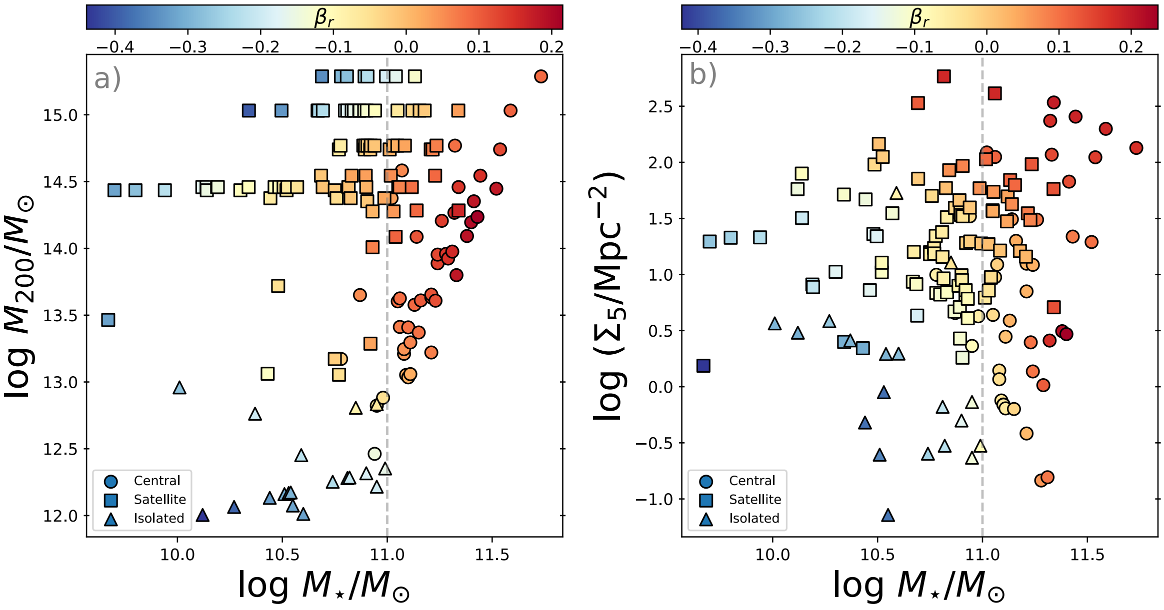

Figure 6. Halo mass $\log M_{200}/M_{\odot}$ and local density $\log(\Sigma_5/\mathrm{Mpc}^{-2})$ as a function of stellar mass, colour-coded by the velocity dispersion anisotropy in spherical coordinates β_r, LOESS smoothed to reveal any mean underlying trend. Central galaxies are shown as circles, satellite galaxies as squares and isolated galaxies as triangles. We find that at fixed halo mass (panel a), β_r increases with increasing stellar mass. Similarly, at fixed stellar mass, β_r increases with increasing halo mass. However, the most radially anisotropic galaxies are in mid-mass haloes. Looking at the local density (panel b), we find that at fixed local density, β_r increases with increasing stellar mass. Similarly, at fixed stellar mass, β_r increases with increasing local density.

thetic galaxies from the EAGLE and HYDRANGEA cosmological hydrodynamic simulations, confirmed the primary dependence of λ_{Re} on stellar mass, but find a weak, secondary dependence on environment so that, at fixed stellar mass ($\log M_{\star}/M_{\odot} \sim 11.25$), central galaxies have lower values of $\lambda_{Re,EO}$, compared to satellite galaxies, in agreement with our results. Choi et al. (2018), with Horizon-AGN simulation data, found a weak trend between the spin parameter and environment, so that galaxies in denser environments (higher-mass haloes) rotate more slowly. They note that the trend is driven by satellite galaxies. Although we do not see a trend with halo mass,

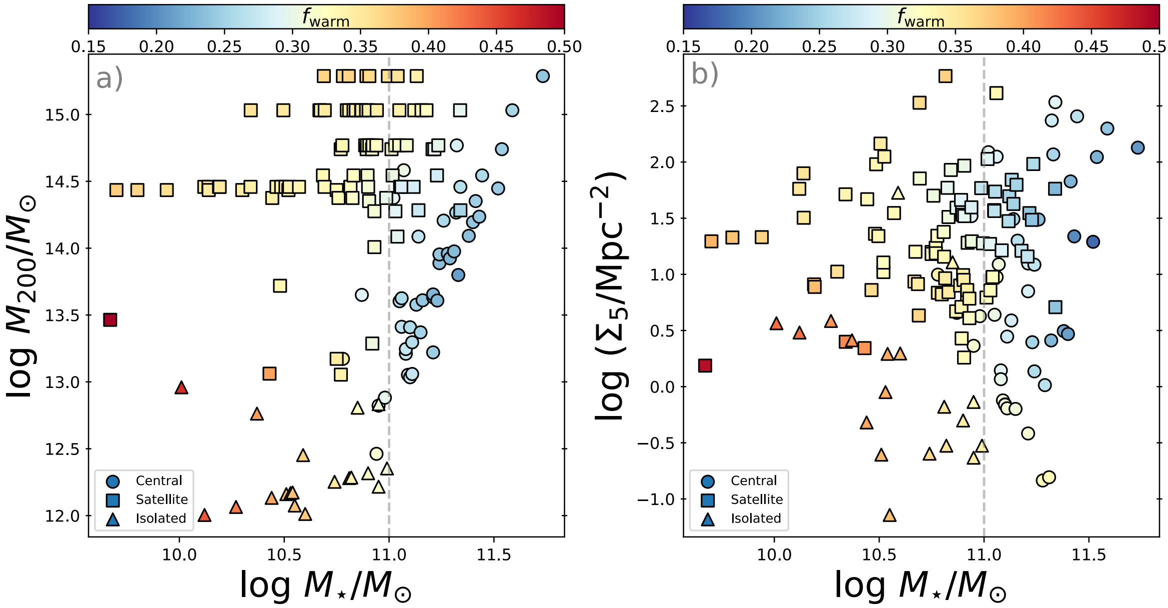

Figure 7. Halo mass log $M_{200}/M_\odot$ and local density $\log(\Sigma_5/{\rm Mpc}^{-2})$ as a function of stellar mass, colour-coded by the fraction of warm orbits, LOESS smoothed to reveal any mean underlying trend. Central galaxies are shown as circles, satellite galaxies as squares and isolated galaxies as triangles. We find suggestions that at fixed stellar mass, galaxies with stellar mass below log $M_\star/M_\odot \sim 11$ have lower fractions of warm orbits with increasing halo mass (panel a) and increasing local density (panel b).

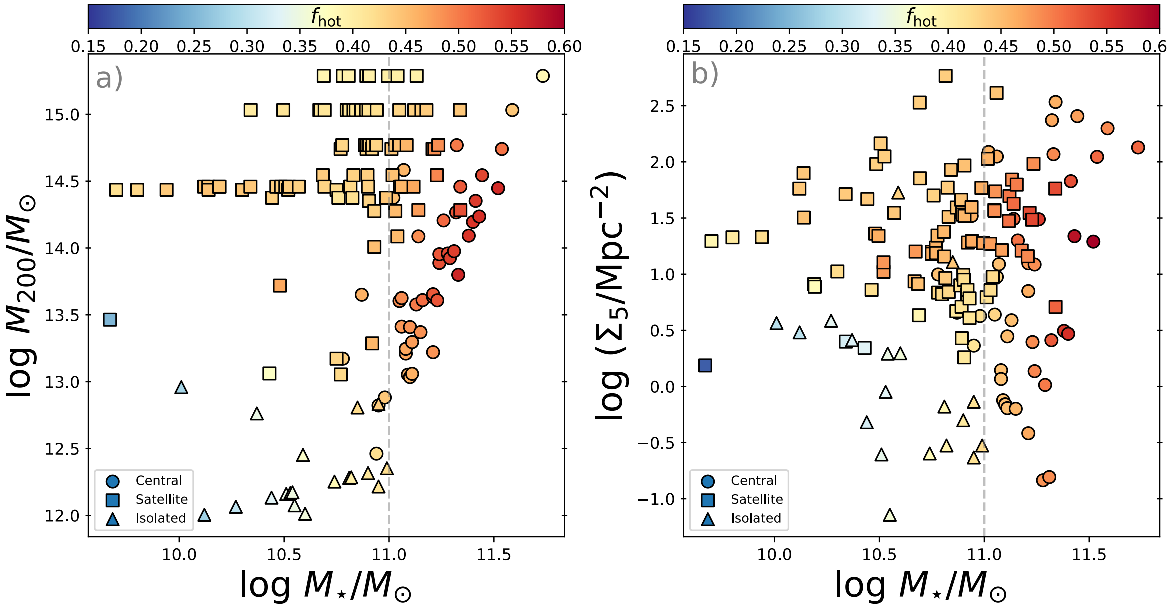

Figure 8. Halo mass log $M_{200}/M_\odot$ and local density $\log(\Sigma_5/{\rm Mpc}^{-2})$ as a function of stellar mass, colour-coded by the fraction of hot orbits, LOESS smoothed to reveal any mean underlying trend. Central galaxies are shown as circles, satellite galaxies as squares and isolated galaxies as triangles. We find suggestions that at fixed stellar mass, galaxies with stellar mass below log $M_\star/M_\odot \sim 11$ have higher fractions of hot orbits with increasing halo mass (panel a) and increasing local density (panel b).

we do see a similar trend with local density. This difference is likely explained by the fact that most of our satellite galaxies are in cluster environments, while there are fewer group satellite galaxies present in our sample for a clear comparison. In their simulations, Choi et al. (2018) found that galaxy mergers (both major and minor) appear to be the main cause of the spin changes for the majority of the central galaxies, while satellite galaxies are more likely to undergo a spin-down from non-merger tidal perturbation (due to high-speed encounters).

4.2 Intrinsic shape

We find that, in general, central galaxies are more likely to be triaxial ($T_{Re} > 0.3$) than satellite and isolated galaxies: 14% ± 5% of central galaxies compared to 7% ± 3% and 5% ± 4% of satellite and isolated galaxies, respectively. However, at fixed stellar mass, there is no significant difference in the mean triaxiality of central, satellite and isolated galaxies (Fig. 3, panel b). This is consistent with previous observations by Jin et al. (2020), who do not find any significant differences between the intrinsic shapes of galaxies in the MaNGA sample, when divided into central and satellite galaxies.

We find that central galaxies have a wider range in shapes, being less axisymmetric than satellite or isolated galaxies. No clear trend of galaxy shape is observed with halo mass or local density. These results are consistent with van den Bosch et al. (2008b), who analysed the colours and concentrations of SDSS galaxies and found no difference in the shape of galaxies as a function of halo mass.

Galaxies with different shapes are predicted to have evolved along different paths. For example, the simulations of Jesseit et al. (2009) and Moody et al. (2014) showed that minor mergers led to flatter remnants (lower q) and higher triaxiality than major mergers. The most triaxial galaxies are usually formed by sequential mergers or re-mergers (Moody et al. 2014). Similarly, Taranu et al. (2013) found that simulations of multiple dry minor mergers usually led to triaxial systems. Lagos et al. (2022) used mock observations of galaxies in the EAGLE simulation to predict that flat (low q) slow-rotating galaxies are preferentially formed from major mergers; whereas round slow-rotating galaxies are formed from minor or very minor mergers; and prolate slow-rotating galaxies from gas-poor mergers. They also found that flat and prolate galaxies are more common among satellite galaxies in massive haloes (with $M_{200} > 10^{13.6} M_{\odot}$).

These simulations would suggest that the central galaxies in our sample are consistent with having undergone multiple minor mergers, leading to more triaxial shapes. The satellite galaxies in our sample would have evolved from different paths: slow-rotating, oblate axisymmetric, satellite galaxies could be consistent with having undergone gas-rich major mergers or no mergers and interactions with the central galaxy or the tidal field of the host halo; slow-rotating triaxial/prolate satellite galaxies are consistent with gas-poor minor mergers; and fast-rotating satellite galaxies are consistent with having evolved through a channel dominated by gas accretion, bulge growth and quenching, leading to more oblate and flat shapes. Isolated galaxies, being in general very close to oblate axisymmetric systems, are consistent with a scenario where very few (gas-rich) or no mergers, have affected their evolution.

4.3 Velocity anisotropy

We find that the global population of central galaxies is in general radially anisotropic or close to isotropic (with average $\beta_r \sim 0.1$; Fig. 3, panel c), while satellite galaxies have average β_r values that are slightly negative (~ -0.3; mildly tangentially anisotropic), and isolated galaxies are tangentially anisotropic at all stellar masses (average $\beta_r \sim -0.5$) . Looking at the correlation between the velocity anisotropy parameter β_r and the environmental proxies, we find a weak correlation with local density (Fig. 6), so that, at fixed stellar mass, galaxies (with stellar mass $\log M_{\star}/M_{\odot} < 11$) in higher local densities have greater values of β_r. However, we note that the most radially anisotropic galaxies are in mid-mass haloes and halo mass (Fig. 6). This might be due to the cluster population being dominated by satellites, while central galaxies (which are generally more radially anisotropic), are only a small fraction of the sample presented here (8%).

Simulations show that mergers can have a substantial effect on the anisotropy of the resulting galaxy (Dekel et al. 2005), and a higher fraction of stars accreted from mergers is connected to greater radial anisotropy, while tangential anisotropy is seen only for galaxies with high fractions of stars formed in-situ (Wu et al. 2014). Since galaxies in group environments are predicted to have experienced a greater number of interactions compared to those in less dense environments, an increased rate of mergers would explain the increase in β_r that we see with increasing halo mass and local density.

Bournaud et al. (2007) found, studying galaxies in N-body simulations, that elliptical-like galaxies formed in multiple minor mergers tend to have larger radial anisotropy than those of similar mass formed in one single merger. This is consistent with the central galaxies in our sample, which show higher values of velocity anisotropy, having undergone multiple minor mergers during their evolution. The satellite and isolated galaxies, which both show lower values of velocity anisotropy, could be formed with fewer or no minor mergers, or gas-rich major mergers, so that they have greater fractions of stars formed in-situ.

4.4 Orbital components

We show the fractions of the warm and hot orbital components, according to their orbit circularity distribution components within $1R_e$, as a function of stellar mass and environment in Fig. 7 and 8. We do not see any significant trend with either halo mass or local density above $\log M_{\star}/M_{\odot} > 11$. However, there is a marginal trend of the fractions of orbits with environment for galaxies with stellar masses below $\log M_{\star}/M_{\odot} \sim 11$, so that galaxies in lower-mass haloes and lower local densities have higher fractions of warm orbits and lower fractions of hot orbits than higher-mass haloes and higher local densities. Central galaxies, at fixed stellar mass, have fewer stars on warm orbits, and large fractions of hot orbits at all stellar masses, but are otherwise consistent with satellite galaxies.

Our results are in general agreement with results from Schwarzschild model fits to early-type galaxies in the MaNGA survey by Jin et al. (2020). They do not find any significant differences between the orbital components of central and satellite galaxies. When considering the local density environments (indicated by neighbour counts), they found that galaxies that have higher neighbour counts tend to have more hot orbits, consistent with the trend that we see for galaxies in different local densities.

The suggestions we find seem to suggest that, while halo mass and local density might have an effect on lower mass galaxies ($\log M_{\star}/M_{\odot} < 11$), galaxy designation (central/satellite/isolated) is more important for higher-mass galaxies. Similar suggestions of stronger trends with environment for lower-mass galaxies are also found by Turner et al. (in prep), in a sample of 7117 simulated galaxies from EAGLE simulation (Schaye et al. 2015) and 3724 observed galaxies from the GAMA survey (Driver et al. 2011).

The suggestions of orbital fraction trends with halo mass and local density that we see for lower-mass galaxies could be connected with the fraction of accreted stars. The cosmological zoom simulations of Röttgers et al. (2014) found that the accreted star component, having fallen in from all directions, is expected to have more radial orbits, while galaxies with more "late" star-formation formed in-situ due to gas accretion or gas-rich mergers, show a higher fraction of circular orbits. Since the accretion of stars (at low redshift) becomes more important for massive systems (e.g. Guo & White 2008; Oser et al. 2010; Naab et al. 2014), we expect massive galaxies to have a higher fraction of stars on hot orbits. Clauwens et al. (2018) studied a sample of galaxies in the EAGLE simulation and found a sharp transition from galaxies dominated by in-situ star-formation to galaxies dominated by ex-situ star-formation at similar masses ($\log M_\star/M_\odot \geq 11$). This is consistent with empirical results from the GAMA survey (Robotham et al. 2014), which show that the stellar mass assembly in galaxies above $10^{11} M_\odot$ is dominated by galaxy mergers. Clauwens et al. (2018) also found that galaxies dominated by in-situ star-formation could be more influenced by non-merger induced tidal perturbations due to their environment, compared to ex-situ dominated galaxies.

The suggestions of weak trends of the orbital fractions with environment for lower-mass galaxies is an interesting indication that needs further study, using a larger sample with a more homogeneous distribution in stellar mass and environment in order to be confirmed.

4.5 Evolutionary scenarios

Early-type galaxies show complicated structures in their kinematic maps, but their kinematics can be broadly separated into two classes, fast- and slow-rotating galaxies (for a recent statistical analysis see: van de Sande et al. 2021b). According to Cappellari (2016), these two classes also represent two major channels of galaxy formation. In this representations, fast-rotating galaxies start as star-forming disc galaxies and evolve through a set of processes dominated by gas accretion, bulge growth and quenching. By comparison, slow-rotating galaxies assemble near the centre of massive haloes via intense star formation at high redshift, and evolve from a set of processes dominated by gas-poor mergers, resulting in more triaxial shapes. These galaxies are the most massive.

Simulations suggest that there are multiple pathways to creating galaxies in the various kinematic classes (e.g. Naab et al. 2014). For example, one effective way of transforming the kinematics of galaxies is via galaxy mergers (e.g. Jesseit et al. 2009; Di Matteo et al. 2009; Bois et al. 2011; Naab et al. 2014; Penoyre et al. 2017; Choi & Yi 2017; Lagos et al. 2017, 2018b). For example, Naab et al. (2014) and Lagos et al. (2018a) found that gas poor mergers are an effective way to decrease λ_{Re}, but also a series of minor mergers or a single major merger can have a similar effect (Naab et al. 2014; Choi & Yi 2017; Schulze et al. 2018; Lagos et al. 2018a).

Our results from Santucci et al. (2022) indicate that the internal structures of galaxies are dominated by the physical processes associated with the growth of stellar mass and are in general agreement with the two formation channels proposed by Cappellari (2016), where the evolution of massive galaxies is dominated by mergers, leading to the spin-down of the systems. However, we also see intriguing evidence for a connection between galaxy evolution and environment. We find suggestions of a trend of the orbital fractions with environment, for lower-mass galaxies, so that galaxies in low-mass haloes (or low local densities) are more rotationally-supported (axisymmetric oblate-like galaxies, with tangential anisotropy, higher values of $\lambda_{Re,EO}$, higher fractions of warm orbits and lower fractions of hot orbits) than galaxies in higher-mass haloes (higher local densities).

Our results suggest two different ways in which environment can affect galaxy evolution. This seems to depend on the galaxy's stellar mass, with a transition at $\log M_\star/M_\odot \sim 11$. This transition mass is also consistent with the sharp transition from in-situ dominated galaxies to ex-situ dominated galaxies found by Clauwens et al. (2018) and with the transition mass ($\log M_\star/M_\odot \sim 11.2$) Cappellari (2016) proposed to mark the increase in the slow-rotating population.

In the scenario suggested by our results, high-mass galaxies (with $\log M_\star/M_\odot > 11$) evolve from a set of sequential mergers (mostly minor), where the fraction of accreted stars is connected to their internal structure: these galaxies are generally pressure supported, with a high fraction of hot orbits, radial anisotropy and more triaxial shape. In our analysis, these galaxies show differences in structure depending on whether they are central, satellite or isolated galaxies, with central galaxies being the slowest-rotating, radially anisotropic galaxies. This picture is consistent with central galaxies having undergone a high number of mergers, in particular minor mergers, that led to a spin-down and to their present-day structure (e.g. Bournaud et al. 2007; Choi et al. 2018; Lagos et al. 2022).

In contrast, galaxies with stellar masses below $\log M_\star/M_\odot \sim 11$ are consistent with being more influenced by non-merger induced tidal perturbations due to their environment. High-speed encounters are more probable in higher-density environments and they can lead to a spin-down of the galaxy and can induce changes in their structures. In our analysis, we see suggestions of these effects in both the velocity anisotropy, the orbital fractions and the edge-on spin-parameter $\lambda_{Re,EO}$, so that at fixed stellar mass, galaxies in low local densities have more tangential velocity anisotropy, higher fractions of warm orbits, lower fractions of hot orbits and are more tangentially supported than galaxies in higher local densities. Suggestions of similar trends are also found with halo mass, but they are less clear, likely because the low-stellar mass / low-halo mass region is not well sampled.

The suggestions pointing to the environment affecting the structure of lower mass galaxies are very interesting. Exploring these results further needs a larger sample, covering a better-sampled range in both stellar mass and environment. We predict the sample size needed in order to observe correlations in these parameters that are significant at the 3-σ level. To do this, we create mock-SAMI galaxies by adding random scatter to the galaxy properties found in this analysis, assuming that the suggestions of correlations we observe are true. We find that we need at least 1500 galaxies (a ~10x increase in sample size) in order to find correlations significant at the 3-σ level. The upcoming Hector galaxy survey (Bryant et al. 2016, 2020), with over 15000 total galaxies, would be the ideal sample with which to test the intriguing conclusions presented here. Undertaking similar analysis in galaxies at higher redshifts (e.g. using the MAGPI survey - Foster et al. 2021) would also help to isolate the evolutionary effect of environment on the stellar kinematics of galaxies.

5 CONCLUSIONS

Using intrinsic galaxy properties derived from building Schwarzschild models, we explore the correlation between the intrinsic shape, velocity anisotropy, orbital components and spin parameter and four environmental proxies: central, satellite or isolated designation, halo mass and local 5^{th} nearest neighbour galaxy density. Our sample consists of 153 galaxies from the SAMI Galaxy Survey, with stellar masses ranging from $9.5 < \log(M_\star/M_\odot) < 12$. Our key findings are:

- Central galaxies (with stellar mass $\log M_\star/M_\odot > 11$) have lower values of $\lambda_{Re,EO}$ than satellite galaxies of similar stellar mass (Fig. 3, panel a) and galaxies in higher local densities show lower values of $\lambda_{Re,EO}$, at fixed stellar mass (Fig. 5).
- At fixed stellar mass, there is no significant difference in the mean triaxiality of central, satellite and isolated galaxies or for galaxies in different environments (Fig. 3, panel b).
- Central galaxies are generally radially anisotropic, while satellite and isolated galaxies are mostly supported by tangential anisotropy (Fig. 3, panel c). The velocity anisotropy parameter, β_r,

shows a weak correlation with environment: in particular with local density (Fig. 6), so that at fixed stellar mass, galaxies in higher local densities have greater values of β_r.

- We do not see any significant trend in the orbital fractions within $1R_e$ with either halo mass or local density, above $\log M_\star/M_\odot > 11$. We find interesting suggestions of trends in the fractions of orbits with environment for galaxies with stellar masses below this, so that galaxies in lower-mass haloes (or less dense local environments) have higher fractions of warm orbits and lower fractions of hot orbits than galaxies in higher-mass haloes (or denser local environments), as shown in Figs. 7 to 8.

The results presented here support a scenario where environment plays a role in shaping present-day galaxies, and that role is secondary to stellar mass. In particular, we find suggestions consistent with the picture that the evolution of high-mass galaxies ($\log M_\star/M_\odot > 11$) is merger-driven, with differences in their structure depending on whether they are central, satellite or isolated galaxies. The evolution of lower-stellar mass galaxies ($\log M_\star/M_\odot < 11$), on the other hand, is consistent with being affected by non-merger tidal perturbations, so that galaxies in denser environments show different structures compared to galaxies in less dense environments.

ACKNOWLEDGEMENTS

The SAMI Galaxy Survey is based on observations made at the Anglo-Australian Telescope. The Sydney-AAO Multi-object Integral field spectrograph (SAMI) was developed jointly by the University of Sydney and the Australian Astronomical Observatory. The SAMI input catalogue is based on data taken from the Sloan Digital Sky Survey, the GAMA Survey and the VST ATLAS Survey. The SAMI Galaxy Survey is supported by the Australian Research Council center of Excellence for All Sky Astrophysics in 3 Dimensions (ASTRO 3D), through project number CE170100013, the Australian Research Council center of Excellence for All-sky Astrophysics (CAASTRO), through project number CE110001020, and other participating institutions. The SAMI Galaxy Survey website is http://sami-survey.org/.

GS acknowledges support of an Australian Government Research Training Program (RTP) Scholarship and of an Australian Research Council Discovery Project (DP210101945) funded by the Australian Government. SB acknowledges funding support from the Australian Research Council through a Future Fellowship (FT140101166). JvdS acknowledges support of an Australian Research Council Discovery Early Career Research Award (project number DE200100461) funded by the Australian Government. RMcD acknowledges funding support via an Australian Research Council Future Fellowship (project number FT150100333). JBH is supported by an ARC Laureate Fellowship FL140100278. The SAMI instrument was funded by Bland-Hawthorn's former Federation Fellowship FF0776384, an ARC LIEF grant LE130100198 (PI Bland-Hawthorn) and funding from the Anglo-Australian Observatory. JJB acknowledges support of an Australian Research Council Future Fellowship (FT180100231). M.S.O. acknowledges the funding support from the Australian Research Council through a Future Fellowship (FT140100255). GvdV acknowledges funding from the European Research Council (ERC) under the European Union's Horizon 2020 research and innovation programme under grant agreement No 724857 (Consolidator Grant ArcheoDyn). S.K.Y. acknowledges support from the Korean National Research Foundation (NRF-2020R1A2C3003769).

DATA AVAILABILITY

All observational data presented in this paper are available from Astronomical Optics' Data Central service at https://datacentral.org.au/ as part of the SAMI Galaxy Survey Data Release 3.

Measurements from Schwarzschild models are available contacting the corresponding author.

REFERENCES

Ahn C. P., et al., 2012, ApJS, 203, 21
Bezanson R., van Dokkum P. G., Tal T., Marchesini D., Kriek M., Franx M., Coppi P., 2009, ApJ, 697, 1290
Bland-Hawthorn J., et al., 2011, Optics Express, 19, 2649
Bois M., et al., 2011, MNRAS, 416, 1654
Boselli A., Gavazzi G., 2006, PASP, 118, 517
Bournaud F., Jog C. J., Combes F., 2007, A&A, 476, 1179
Brough S., Tran K. V., Sharp R. G., von der Linden A., Couch W. J., 2011, MNRAS, 414, L80
Brough S., et al., 2013, MNRAS, 435, 2903
Brough S., et al., 2017, ApJ, 844, 59
Bryant J. J., Bland-Hawthorn J., Fogarty L. M. R., Lawrence J. S., Croom S. M., 2014, MNRAS, 438, 869
Bryant J. J., et al., 2015, MNRAS, 447, 2857
Bryant J. J., et al., 2016, in Evans C. J., Simard L., Takami H., eds, Society of Photo-Optical Instrumentation Engineers (SPIE) Conference Series Vol. 9908, Ground-based and Airborne Instrumentation for Astronomy VI. p. 99081F (`arXiv:1608.03921`), doi:10.1117/12.2230740
Bryant J. J., et al., 2020, in Society of Photo-Optical Instrumentation Engineers (SPIE) Conference Series. p. 1144715, doi:10.1117/12.2560309
Bundy K., et al., 2015, ApJ, 798, 7
Cappellari M., 2002, MNRAS, 333, 400
Cappellari M., 2016, ARA&A, 54, 597
Cappellari M., et al., 2007, MNRAS, 379, 418
Cappellari M., et al., 2011a, MNRAS, 413, 813
Cappellari M., et al., 2011b, MNRAS, 416, 1680
Cappellari M., et al., 2013, MNRAS, 432, 1862
Chabrier G., 2003, ApJ, 586, L133
Choi H., Yi S. K., 2017, ApJ, 837, 68
Choi H., Yi S. K., Dubois Y., Kimm T., Devriendt J. E. G., Pichon C., 2018, ApJ, 856, 114
Clauwens B., Schaye J., Franx M., Bower R. G., 2018, MNRAS, 478, 3994
Cortese L., et al., 2019, MNRAS, 485, 2656
Cortese L., Catinella B., Smith R., 2021, Publ. Astron. Soc. Australia, 38, e035
Cretton N., de Zeeuw P. T., van der Marel R. P., Rix H.-W., 1999, ApJS, 124, 383
Croom S., Saunders W., Heald R., 2004, Anglo-Australian Observatory Epping Newsletter, 106, 12
Croom S. M., et al., 2012, Monthly Notices of the Royal Astronomical Society, 421, 872
Croom S. M., et al., 2021, MNRAS,
D'Eugenio F., Houghton R. C. W., Davies R. L., Dalla Bontà E., 2013, MNRAS, 429, 1258
D'Eugenio F., et al., 2021, MNRAS,
De Lucia G., Blaizot J., 2007, MNRAS, 375, 2
Dekel A., Stoehr F., Mamon G. A., Cox T. J., Novak G. S., Primack J. R., 2005, Nature, 437, 707
Di Matteo P., Pipino A., Lehnert M. D., Combes F., Semelin B., 2009, A&A, 499, 427
Driver S. P., et al., 2011, MNRAS, 413, 971
Emsellem E., Monnet G., Bacon R., 1994, A&A, 285, 723

Emsellem E., et al., 2011, MNRAS, 414, 888
Fall S. M., Efstathiou G., 1980, MNRAS, 193, 189
Feldmeier-Krause A., Zhu L., Neumayer N., van de Ven G., de Zeeuw P. T., Schödel R., 2017, MNRAS, 466, 4040
Fogarty L. M. R., et al., 2014, MNRAS, 443, 485
Foster C., et al., 2021, Publ. Astron. Soc. Australia, 38, e031
Gebhardt K., et al., 2003, ApJ, 583, 92
Green A. W., et al., 2018, Monthly Notices of the Royal Astronomical Society, 475, 716
Greene J. E., et al., 2017, ApJ, 851, L33
Guo Q., White S. D. M., 2008, MNRAS, 384, 2
Harborne K. E., van de Sande J., Cortese L., Power C., Robotham A. S. G., Lagos C. D. P., Croom S., 2020, MNRAS, 497, 2018
Hill D. T., et al., 2011, MNRAS, 412, 765
Houghton R. C. W., et al., 2013, MNRAS, 436, 19
Jesseit R., Cappellari M., Naab T., Emsellem E., Burkert A., 2009, MNRAS, 397, 1202
Jimmy Tran K.-V., Brough S., Gebhardt K., von der Linden A., Couch W. J., Sharp R., 2013, ApJ, 778, 171
Jin Y., Zhu L., Long R. J., Mao S., Wang L., van de Ven G., 2020, MNRAS, 491, 1690
Krajnović D., McDermid R. M., Cappellari M., Davies R. L., 2009, MNRAS, 399, 1839
Lagos C. d. P., Theuns T., Stevens A. R. H., Cortese L., Padilla N. D., Davis T. A., Contreras S., Croton D., 2017, MNRAS, 464, 3850
Lagos C. d. P., et al., 2018a, MNRAS, 473, 4956
Lagos C. d. P., Schaye J., Bahé Y., Van de Sande J., Kay S. T., Barnes D., Davis T. A., Dalla Vecchia C., 2018b, MNRAS, 476, 4327
Lagos C. d. P., Emsellem E., van de Sande J., Harborne K. E., Cortese L., Davison T., Foster C., Wright R. J., 2022, MNRAS, 509, 4372
Lawson C. L., Hanson R. J., 1974, Solving least squares problems
Li H., Mao S., Emsellem E., Xu D., Springel V., Krajnović D., 2018, MNRAS, 473, 1489
Liepold C. M., Quenneville M. E., Ma C.-P., Walsh J. L., McConnell N. J., Greene J. E., Blakeslee J. P., 2020, ApJ, 891, 4
Liske J., et al., 2015, MNRAS, 452, 2087
Loveday J., et al., 2015, MNRAS, 451, 1540
Ma C.-P., Greene J. E., McConnell N., Janish R., Blakeslee J. P., Thomas J., Murphy J. D., 2014, ApJ, 795, 158
Moody C. E., Romanowsky A. J., Cox T. J., Novak G. S., Primack J. R., 2014, MNRAS, 444, 1475
Muldrew S. I., et al., 2012, MNRAS, 419, 2670
Naab T., Johansson P. H., Ostriker J. P., 2009, ApJ, 699, L178
Naab T., et al., 2014, MNRAS, 444, 3357
Navarro J. F., Frenk C. S., White S. D. M., 1996, ApJ, 462, 563
Neureiter B., et al., 2021, MNRAS, 500, 1437
Oliva-Altamirano P., et al., 2017, AJ, 153, 89
Oser L., Ostriker J. P., Naab T., Johansson P. H., Burkert A., 2010, ApJ, 725, 2312
Owers M. S., et al., 2017, MNRAS, 468, 1824
Owers M. S., et al., 2019, arXiv e-prints,
Park M.-J., et al., 2019, ApJ, 883, 25
Penoyre Z., Moster B. P., Sijacki D., Genel S., 2017, MNRAS, 468, 3883
Pilawa J. D., Liepold C. M., Delgado Andrade S. C., Walsh J. L., Ma C.-P., Quenneville M. E., Greene J. E., Blakeslee J. P., 2022, ApJ, 928, 178
Poci A., McDermid R. M., Zhu L., van de Ven G., 2019, MNRAS, 487, 3776
Poci A., et al., 2021, A&A, 647, A145
Quenneville M. E., Liepold C. M., Ma C.-P., 2021, ApJS, 254, 25
Quenneville M. E., Liepold C. M., Ma C.-P., 2022, ApJ, 926, 30
Robotham A. S. G., et al., 2011, MNRAS, 416, 2640
Robotham A. S. G., et al., 2014, MNRAS, 444, 3986
Röttgers B., Naab T., Oser L., 2014, MNRAS, 445, 1065
Rusli S. P., et al., 2013, AJ, 146, 45
Rutherford T. H., et al., 2021, ApJ, 918, 84
Sánchez S. F., et al., 2012, A&A, 538, A8
Santucci G., et al., 2020, ApJ, 896, 75
Santucci G., et al., 2022, arXiv e-prints, p. arXiv:2203.03648
Schaye J., et al., 2015, MNRAS, 446, 521
Schulze F., Remus R.-S., Dolag K., Burkert A., Emsellem E., van de Ven G., 2018, MNRAS, 480, 4636
Scott N., et al., 2009, MNRAS, 398, 1835
Scott N., Davies R. L., Houghton R. C. W., Cappellari M., Graham A. W., Pimbblet K. A., 2014, MNRAS, 441, 274
Seth A. C., et al., 2014, Nature, 513, 398
Shanks T., et al., 2015, Monthly Notices of the Royal Astronomical Society, 451, 4238
Sharp R., Birchall M. N., 2010, Publ. Astron. Soc. Australia, 27, 91
Sharp R., et al., 2006, in McLean I. S., Iye M., eds, Society of Photo-Optical Instrumentation Engineers (SPIE) Conference Series Vol. 6269, Society of Photo-Optical Instrumentation Engineers (SPIE) Conference Series. p. 62690G (`arXiv:astro-ph/0606137`), doi:10.1117/12.671022
Sharp R., et al., 2015, MNRAS, 446, 1551
Springel V., Hernquist L., 2005, ApJ, 622, L9
Taranu D. S., Dubinski J., Yee H. K. C., 2013, ApJ, 778, 61
Taylor E. N., et al., 2011, MNRAS, 418, 1587
Thater S., et al., 2017, A&A, 597, A18
Thater S., Krajnović D., Cappellari M., Davis T. A., de Zeeuw P. T., McDermid R. M., Sarzi M., 2019, A&A, 625, A62
Thater S., et al., 2022a, arXiv e-prints, p. arXiv:2205.04165
Thater S., et al., 2022b, MNRAS, 509, 5416
Thomas J., Saglia R. P., Bender R., Thomas D., Gebhardt K., Magorrian J., Corsini E. M., Wegner G., 2007, MNRAS, 382, 657
Tsatsi A., Lyubenova M., van de Ven G., Chang J., Aguerri J. A. L., Falcón-Barroso J., Macciò A. V., 2017, A&A, 606, A62
Vallat R., 2018, The Journal of Open Source Software, 3, 1026
Valluri M., Merritt D., Emsellem E., 2004, ApJ, 602, 66
Vasiliev E., Athanassoula E., 2015, MNRAS, 450, 2842
Vasiliev E., Valluri M., 2020, ApJ, 889, 39
Veale M., Ma C.-P., Greene J. E., Thomas J., Blakeslee J. P., McConnell N., Walsh J. L., Ito J., 2017, MNRAS, 471, 1428
Verolme E. K., et al., 2002, MNRAS, 335, 517
Wang B., Cappellari M., Peng Y., Graham M., 2020, MNRAS, 495, 1958
Wellons S., et al., 2016, MNRAS, 456, 1030
White S. D. M., 1979, MNRAS, 186, 145
White S. D. M., Rees M. J., 1978, MNRAS, 183, 341
Wu X., Gerhard O., Naab T., Oser L., Martinez-Valpuesta I., Hilz M., Churazov E., Lyskova N., 2014, MNRAS, 438, 2701
York D. G., et al., 2000, AJ, 120, 1579
Zhu L., et al., 2018a, MNRAS, 473, 3000
Zhu L., van de Ven G., Méndez-Abreu J., Obreja A., 2018b, MNRAS, 479, 945
Zhu L., et al., 2020, MNRAS, 496, 1579
Zhu L., et al., 2022, arXiv e-prints, p. arXiv:2203.15822
van Dokkum P. G., et al., 2010, ApJ, 709, 1018
van de Sande J., et al., 2017a, MNRAS, 472, 1272
van de Sande J., et al., 2017b, ApJ, 835, 104
van de Sande J., et al., 2021a, MNRAS,
van de Sande J., et al., 2021b, MNRAS, 505, 3078
van de Ven G., van den Bosch R. C. E., Verolme E. K., de Zeeuw P. T., 2006, A&A, 445, 513
van de Ven G., de Zeeuw P. T., van den Bosch R. C. E., 2008, MNRAS, 385, 614
van den Bosch R. C. E., van de Ven G., Verolme E. K., Cappellari M., de Zeeuw P. T., 2008a, MNRAS, 385, 647
van den Bosch F. C., Aquino D., Yang X., Mo H. J., Pasquali A., McIntosh D. H., Weinmann S. M., Kang X., 2008b, MNRAS, 387, 79
van der Marel R. P., Cretton N., de Zeeuw P. T., Rix H.-W., 1998, ApJ, 493, 613

APPENDIX A: ENVIRONMENT-STELLAR MASS PLANE - NATIVE FIGURES

We show the distribution of the edge-on spin parameter $\lambda_{Re,EO}$, β_r, fraction of hot and warm orbits in the halo mass-stellar mass and local density-stellar mass plane in Fig. A1 to A4, without applying a locally weighted regression algorithm.

APPENDIX B: INTRINSIC SHAPE

We show the distribution of galaxy triaxiality in the halo mass-stellar mass and local density-stellar mass plane in Fig. B1. In both cases, we do not find any significant correlation between triaxiality and environment.

APPENDIX C: FRACTION OF COLD AND COUNTER-ROTATING ORBITS

When looking at the fraction of cold orbits of galaxies in different halo masses (Fig. C1) we observe that, for stellar masses below $\log M_\star/M_\odot \sim 11$, galaxies show evidence of a possible additional relationship between the orbital fractions and halo mass so that lower-mass galaxies (below $\log M_\star/M_\odot \sim 11$) in lower-mass haloes (below $\log M_{200}/M_\odot \sim 13.5$) are more likely to have lower fractions of cold orbits. However, we note that the variations in the fractions of cold orbits are small and that our sample does not have many galaxies in the low-stellar mass / low-halo mass region to be able to clearly see a correlation. This suggestion could be connected to satellite galaxies in clusters quenching rapidly and efficiently without undergoing changes in their morphology (e.g. Cortese et al. 2019, Turner et al. in prep), therefore retaining their disc-like components. Above $\log M_\star/M_\odot \sim 11$, any difference in cold orbit fraction between different halo environments disappears. We do not find any additional relationship between the fraction of cold orbits and local density.

We do not find any additional correlation between the fraction of counter-rotating orbits and halo mass or local density (Fig. C2).

This paper has been typeset from a TEX/LATEX file prepared by the author.

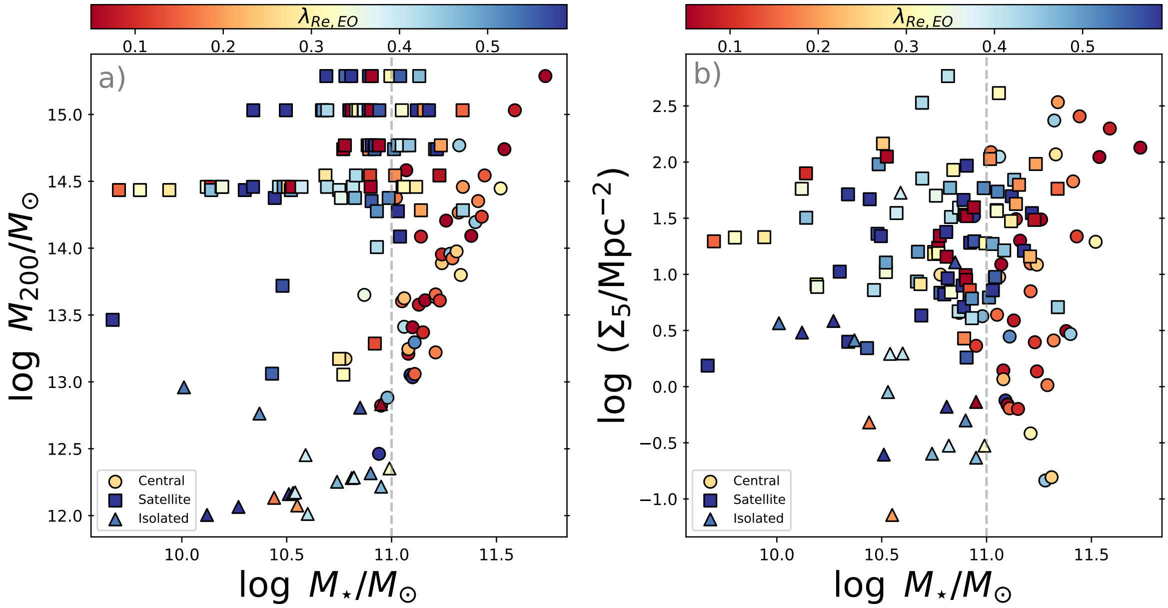

Figure A1. Halo mass log $M_{200}/M_\odot$ and local density $\log(\Sigma_5/\mathrm{Mpc}^{-2})$ as a function of stellar mass, colour-coded by $\lambda_{Re,EO}$. Central galaxies are shown as circles, satellite galaxies as squares and isolated galaxies as triangles.

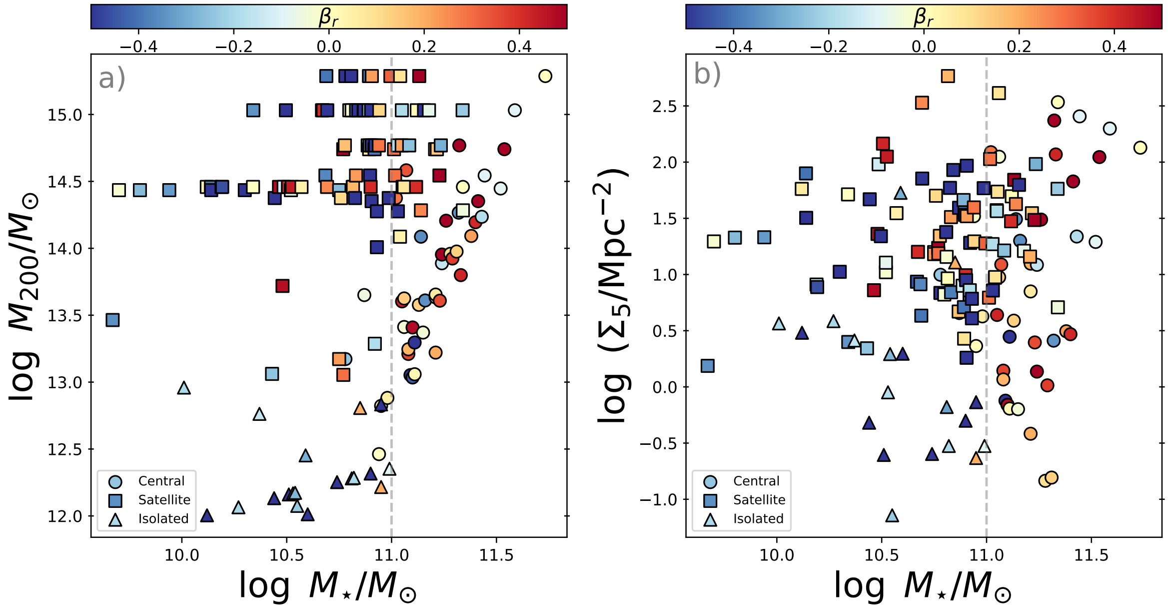

Figure A2. Halo mass log $M_{200}/M_\odot$ and local density $\log(\Sigma_5/\mathrm{Mpc}^{-2})$ as a function of stellar mass, colour-coded by β_r. Central galaxies are shown as circles, satellite galaxies as squares and isolated galaxies as triangles.

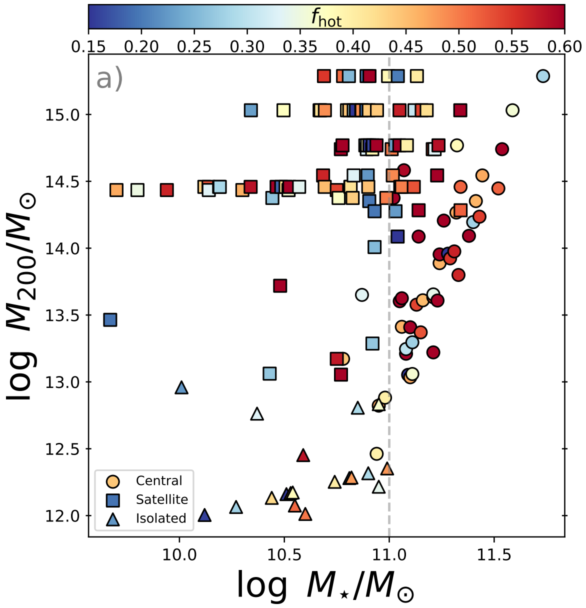

Figure A3. Halo mass log $M_{200}/M_\odot$ and local density $\log(\Sigma_5/{\rm Mpc}^{-2})$ as a function of stellar mass, colour-coded by the fraction of hot orbits. Central galaxies are shown as circles, satellite galaxies as squares and isolated galaxies as triangles.

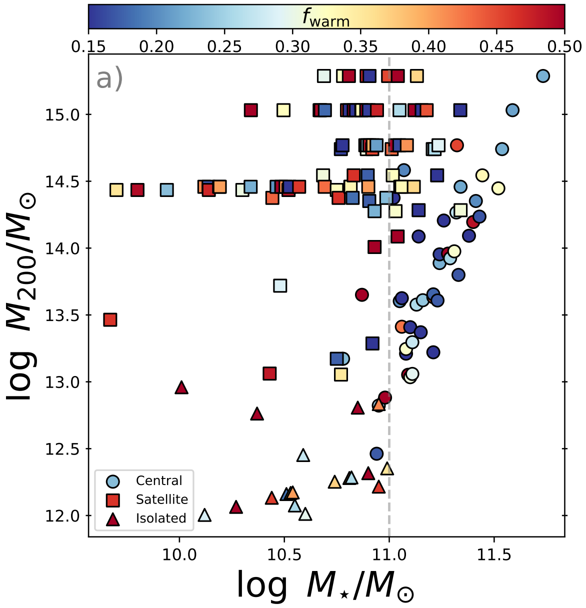

Figure A4. Halo mass log $M_{200}/M_\odot$ and local density $\log(\Sigma_5/{\rm Mpc}^{-2})$ as a function of stellar mass, colour-coded by the fraction of warm orbits. Central galaxies are shown as circles, satellite galaxies as squares and isolated galaxies as triangles.

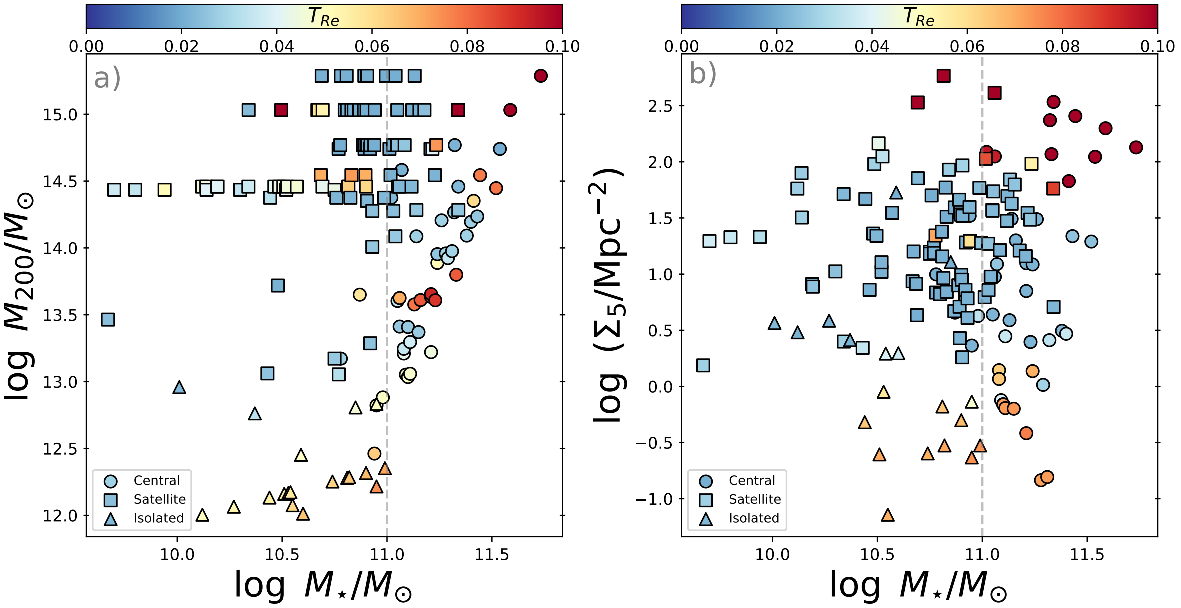

Figure B1. Halo mass log $M_{200}/M_\odot$ and local density $\log(\Sigma_5/\mathrm{Mpc}^{-2})$ as a function of stellar mass, colour-coded by triaxiality, LOESS smoothed to reveal any mean underlying trend. Central galaxies are shown as circles, satellite galaxies as squares and isolated galaxies as triangles. We do not find any significant correlation between triaxiality and environment.

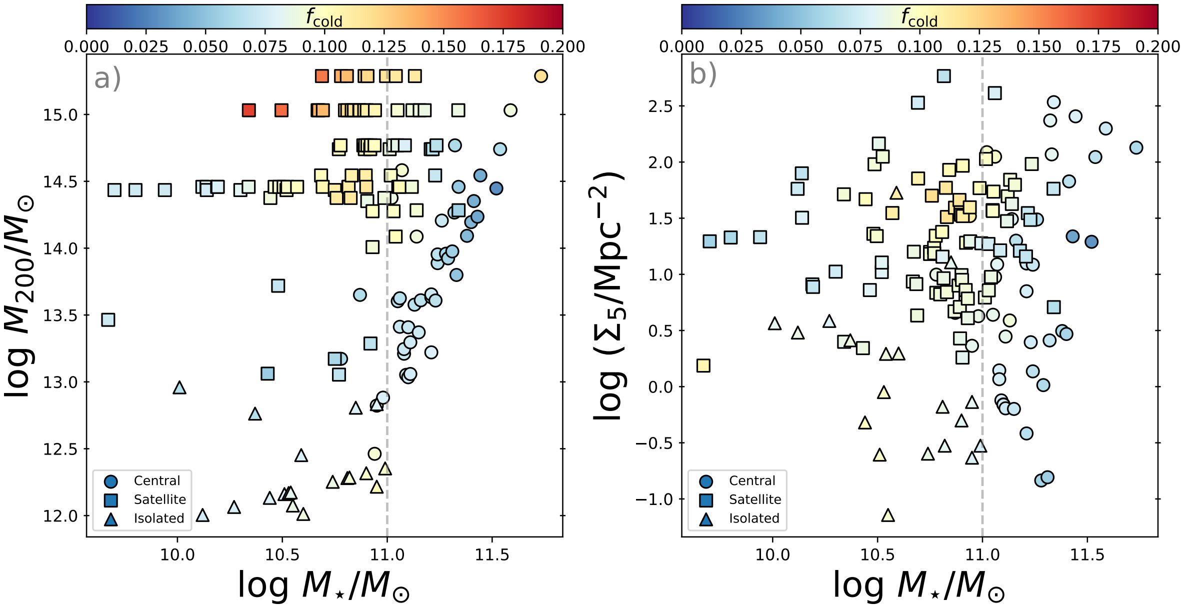

Figure C1. Halo mass log $M_{200}/M_\odot$ and local density $\log(\Sigma_5/\mathrm{Mpc}^{-2})$ as a function of stellar mass, colour-coded by the fraction of cold orbits, LOESS smoothed to reveal any mean underlying trend. Central galaxies are shown as circles, satellite galaxies as squares and isolated galaxies as triangles. We do not find any correlation between the fraction of cold orbits and halo mass (panel a) or local density (panel b).

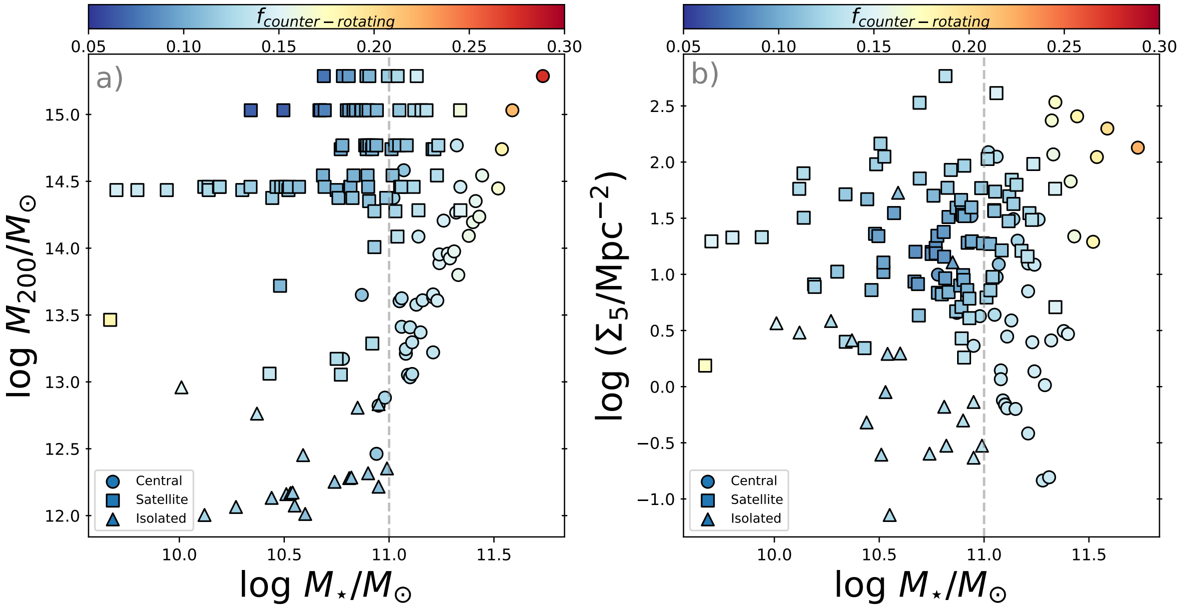

Figure C2. Halo mass log $M_{200}/M_{\odot}$ and local density $\log(\Sigma_5/\mathrm{Mpc}^{-2})$ as a function of stellar mass, colour-coded by the the fraction of counter-rotating orbits, LOESS smoothed to reveal any mean underlying trend. Central galaxies are shown as circles, satellite galaxies as squares and isolated galaxies as triangles. We do not find any correlation between the fraction of counter-rotating orbits and halo mass (panel a) or local density (panel b).